Cryo-EM of cardiac AL-224L amyloid reveals shared features in λ6 light chain fibril folds

Authors: Chad W. Hicks [a,#], Tatiana Prokaeva [b,c], Brian Spencer [b], Shobini Jayaraman [a], Noorul Huda [a], Sherry Wong [b], Hui Chen [c], Vaishali Sanchorawala [b], Francesca Lavatelli [d], Olga Gursky [a,#]

Affiliations:

[a] *Department of Pharmacology, Physiology & Biophysics, Chobanian & Avedisian School of Medicine, Boston University, Boston, MA, USA*

[b] *Amyloidosis Center, Chobanian & Avedisian School of Medicine, Boston University, Boston, MA, USA*

[c] *Department of Pathology and Laboratory Medicine, Chobanian & Avedisian School of Medicine, Boston University, Boston, MA, USA*

[d] *Department of Molecular Medicine, University of Pavia, and Research Area, Fondazione IRCCS Policlinico San Matteo, Pavia, Italy.*

 # Corresponding authors

ORCID ID: Chad Hicks 0000-0002-6040-6227; Olga Gursky 0000-0002-8598-4824

Keywords: Human immunoglobulin mutations; Structural polymorphism; Registry shift with backbone flipping; Amyloid-ligand interactions; Collagen binding to amyloid; short-chain fatty acids.

Abbreviations: AL – amyloid light chain; APR – amyloid-promoting region; CDR – complementarity determining region; C_L – light chain constant domain; cryo-EM – cryogenic electron microscopy; LC – light chain; LC-MS/MS - liquid chromatography tandem mass spectrometry; V_L – light chain variable domain.

ABSTRACT

In amyloid light chain (AL) amyloidosis, aberrant monoclonal antibody light chains (LCs) deposit in vital organs causing organ damage. Each AL patient features a unique LC. Previous cryogenic electron microscopy (cryo-EM) studies revealed different amyloid structures in different AL patients. How LC mutations influence amyloid structures remains unclear. We report a cryo-EM structure of cardiac AL-224L amyloid (2.92 Å resolution) from λ6-LC family, which is overrepresented in amyloidosis. Comparison with λ6-LC structures from two other patients reveals similarities in amyloid folds. Mutation-induced structural differences in AL-224L include altered C-terminal conformation with an exposed ligand-binding surface; an enlarged hydrophilic pore with orphan density; and altered steric zipper registry with backbone flipping, which likely represent general adaptive mechanisms in amyloids. The results suggest shared features in λ6-LC amyloid folds and reveal how mutation-induced structural changes influence amyloid-ligand interactions in a patient-specific manner.

INTRODUCTION

AL amyloidosis accounts for nearly ¾ of all systemic amyloid diseases. This debilitating life-threatening systemic disorder is caused by the deposition of monoclonal immunoglobulin LCs as extracellular amyloid fibrils in vital organs, particularly heart and kidney[1]. Annually, the disease afflicts 10-12 new patients per million[2,3]. Cardiac AL amyloidosis is detrimental to patients' prognosis and is lethal if untreated. Current treatments involve chemotherapy and bone marrow transplantation to eliminate the abnormally proliferating B-cell clone that overproduces the aberrant LC protein, along with proteasome inhibitors, immunomodulatory agents, and monoclonal antibodies to eliminate the LC[2–4]. Transplantation of the afflicted organ (kidney, heart) and supportive treatments are also available to extend the patient's life and improve the quality of life. However, these treatments are not suited for all patients. New therapies are being developed, including small-molecule LC stabilizers and CRISPR-based approaches targeting the aberrant LC generation[3–5]. These efforts are complicated by the extreme variability of antibodies stemming from gene recombination and somatic hypermutations; as a result, each amyloidosis patient features a unique fibril-forming LC[6–8]. Since the pathological role of fibrils in AL and other forms of systemic amyloidoses is well established[4], understanding molecular underpinnings for amyloid fibril formation, structure and biological properties may help guide the development of much-needed amyloid-targeting therapies.

In the normal polyclonal LC repertoire, κ-LC and λ-LC proteins are found at a 2:1 ratio, yet AL amyloidosis is most frequently associated with the overexpression of λ-LCs[9]. Moreover, *IGLV6-57* gene segment encoding the variable domain (V_L) of λ6-LCs is expressed in ~2% of the polyclonal λ-LC repertoire but accounts for ~25% of AL amyloid cases[10,11]. This study is focused on the λ6-LC protein subfamily.

Native LC proteins (~25 kDa) share a common two-domain architecture consisting of the N-terminal variable (V_L) and C-terminal constant (C_L) domains joined by a short flexible linker (J-region); each domain acquires a β-sandwich immunoglobulin fold. AL deposits always contain V_L, either as a full-length LC or LC fragments[12,13]. Most LC mutations in AL patients cluster in V_L in or near three antigen-binding loops, called complementarity-determining regions (CDRs). Amyloidogenic mutations have been reported to destabilize the native structure in V_L, to perturb the protective domain-domain interactions in LC monomers or dimers, to increase protein dynamics/exposure in sensitive regions (including the interdomain linker, the amyloid-promoting regions (APRs) in V_L, and the proteolysis-prone segments in C_L), or to stabilize the amyloid structure[5,14–21]. However, oftentimes it is unclear how amyloidogenic mutations promote the misfolding of native LCs to amyloid structure. Moreover, the major triggers of misfolding are different for different LCs[22,23], suggesting different amyloidogenic pathways for different patients.

This idea is supported by the cryo-EM structural studies; 12 structures of tissue-derived amyloid fibrils formed by LCs from λ1, λ3, and λ6 sub-families are currently available[13,18,21,23–26]. The amyloid folds in these fibrils drastically differ from the native immunoglobulin fold. Importantly, fibrils from the same organ of different patients show different amyloid structures[23], while fibrils from different organs of the same patient show similar structures[24]. Since each AL patient features a unique set of mutations in the fibrillar LC, these results suggest that LC mutations are critical for determining amyloid fold.

Nevertheless, cryo-EM structures of several λ3-LCs from different patients show some similarities, suggesting that amyloids from the same protein subfamily can be structurally related[13,23]. Despite this recent progress, the paucity of the AL amyloid fibril structures and their diversity prohibit using machine-learning tools such as AlphaFold[26] to predict new amyloid structures of LCs based on their amino acid sequences.

Of the available LC fibril structures, only two proteins are from the λ6-LC subfamily: amyloids from the heart and kidney of patient AL55 (AL-Base number AL55, PDB ID: 6HUD and 8CPE)[24,26] and amyloid from the heart of a patient AL-9ELS (PDB ID: 9ELS)[21]. Cardiac and renal AL55 amyloids have similar structures that differ from the AL-9ELS structure. To expand the available structural repertoire of λ6-LC amyloids, we determined a cryo-EM structure of cardiac AL-224L amyloid (PDB ID: 9OKA). This structure shares key similarities but also shows important mutation-induced structural differences with AL55 and AL-9ELS amyloids. Interestingly, AL-224L amyloid shows an altered C-terminal conformation with an exposed ligand-binding surface that may bind collagen; an enlarged hydrophilic pore with orphan density; and altered steric zipper registry with backbone flipping. These results suggest shared structural features for λ6-LC amyloids, show how AL mutations influence amyloid structure, and reveal how this structural variability alters amyloid-ligand interactions that define the biological properties of amyloids.

RESULTS

Analysis of AL-224L amyloid deposits and the extracted fibrils

Amyloid fibrils were extracted from the explanted heart of a previously reported 63-year-old female patient AL-224 with AL amyloidosis[28] (Table S1). Tissue analysis by Congo red staining and light microscopy indicated amyloid (Fig. S1A,B). Immunogold transmission electron microscopy showed reactivity with λ-LC antibody (Fig. S1C,D). The *IGL* gene sequence derived from the patient's bone marrow showed that AL-224L protein belonged to the λ6-LC family and was encoded by the *IGLV6-57*01, IGLJ2*02,* and *IGLC2*02* germline genes.

Liquid chromatography tandem mass spectrometry (LC-MS/MS) of fibril extracts confirmed the sequence identity of the amyloid-forming and the bone marrow-derived LCs and showed 74% peptide coverage in AL-224L residues 1-192, which encompass V_L and a part of C_L domain (Figs. 1A, S2). 2D-PAGE of fibril extracts showed two most abundant species at 15 kDa (Fig. S2A-B). LC-MS/MS of these species detected AL-224L residues 1-116 (Fig. S2C) confirming that the fibrils contained the entire V_L domain. Similar to previous reports[12,28,29], 2D western blot detected additional low-abundance species representing the full-length and fragmented LC (Fig. S2A-B).

LC-MS/MS identified additional proteins in the fibril extracts; Table S2 lists top 30 proteins. AL-224L was prevalent based on normalized spectral abundance factors. Other proteins, including amyloid signature proteins (apoE, apoA-IV) and three chains of collagen VI (ColVI), were identified with lower abundance. ColVI showed similar abundance in prior studies of cardiac λ3-AL59 fibrils that were extracted using similar protocols and contained ColVI bound to LC fibrils[13].

The native structures of LC and its V_L domain (Fig. 1B,C) differ drastically from their structure in an amyloid fibrils[13,18,21,23–26]. To obtain high-resolution structural information on AL-224L fibrils, we used cryo-EM (Fig. S3). While cryo-EM data of amyloid fibrils are typically processed using Relion[30], we performed cryo-EM data processing exclusively in CryoSPARC. Only two other investigations have determined amyloid structures using CryoSPARC[31,32]. To our knowledge, our structure of AL-224L amyloid has the highest global resolution of all similar structures processed in CryoSPARC. Methods provide detailed information of our data processing workflow to assist future investigations.

Cryo-EM micrographs showed long twisted AL-224L fibrils with either single- or double-filament morphology (Fig. 2A). 2D classification showed that ~75% of the fibril segments were single-filament with a helical crossover of approximately 700 Å, while ~25% were double-filament (Fig. 2B). We determined the cryo-EM structure of the single-filament polymorph to a resolution of 2.92 Å (Table 1 and Fig. S4A), which showed clear side-chain densities (Fig. S4B-D) and β-sheet separation (Fig. S4E). Local resolution estimation of the cryo-EM map showed a well-resolved central core at ~2.5 Å and less resolved peripheral parts at ~3.5 Å (Fig. 2C). Symmetry search analysis of the single-filament structure revealed a helical rise of 4.86 Å and a twist of 1.20°. Analysis of the corrugation in the EM density of backbone carbonyl atoms suggested a right-handed twist (Fig. S5). We were unable to determine the double-filament structure, likely due to an insufficient amount of data for this polymorph.

148

149 **Cardiac λ6-LC amyloids from different patients share key structural features**

150 Like in other patient-derived AL fibrils, the fibril core in AL-224L contains misfolded V_L
151 domains in a parallel in-registry cross-β-sheet conformation (Fig. 3). The β-strands are
152 linked via intermolecular hydrogen bonds running along the fibril z-axis while the side
153 chains pack via steric zippers in the x-y plane[33,34].

154 The AL-224L V_L domain contains 111 amino acids, while its AL55 counterpart contains 110
155 amino acids that differ from AL-224L in 13 point substitutions and 1 insertion (Fig. 1A).
156 Surprisingly, the two amyloids show similar folds consisting of a central N-terminal "snail
157 shell-shaped" segment[26] (NT-segment, residues 1-41 in AL-224L and 1-34 in AL55)
158 enclosed by a C-terminal C-shaped segment (CT-segment, residues 59-104 in AL-224L
159 and 66-106 in AL55) (Fig. 4A,B). These structured antiparallel segments are covalently
160 linked by the canonical disulfide, C22-C91. This ordered structure is flanked by two
161 disordered segments seen in the cryo-EM map as diffuse densities, one encompassing
162 the CDR2-containing linker between the NT- and CT-segments (residues 42-58 in AL-224L
163 and 35-65 in AL55) and the other extending C-terminally from V_L into the proximal end of
164 C_L (residues 105-116 in AL-224L and 107-119 in AL55) (Figs. 3B,C, 4A,B). The ordered
165 C-terminal tail (CT-tail, residues 95-104 in AL-224L and 95-106 in AL55) is repositioned:
166 the AL-224L CT-tail extends straight around the NT-segment while the AL55 CT-tail makes
167 two ~90° turns and folds back on itself (Fig. 4A,B).

168 The AL-9ELS V_L domain contains 111 amino acids[21] that differ from AL-224L in 11 point
169 substitutions (Fig. 1A). Like AL-224L and AL-55, the AL-9ELS amyloid structure contains
170 antiparallel well-ordered NT- and CT-segments (residues 1-40 and 61-112) connected by
171 the disordered CDR2-containing linker and by the C22-C91 disulfide (Fig. 5). The NT-
172 segment in the AL-9ELS amyloid is not snail-shell shaped, like in AL-224L and AL55.
173 Rather than occupying a sequestered central position, AL-9ELS segment 1-14 is
174 repositioned towards the structural periphery and rotates by ~180° to encircle residues
175 96-101 of the CT-segment (Fig. 5C). In contrast with AL-224L, the AL-9ELS CT-tail
176 (structured residues 95-112) folds back on itself.

177 All three λ6-LC amyloids contain a buried salt bridge, K16-D95 (E95 in AL-9ELS) (Figs.
178 4C,D, 5)[21,26]. This stabilizing salt bridge and the C22-C91 disulfide help maintain the
179 antiparallel orientation and local registry of the juxtaposed NT- and CT-segments.

180 V_L domain of LCs typically harbors six amyloid-promoting regions (APRs)[19]. Six APRs
181 were predicted by at least three different methods for AL-224L (Fig. 1A) and other λ6-LCs
182 using the sequence-based consensus algorithm AmylPred2[35]. Four APRs are in the
183 structured segments of AL224L, AL55, and AL-9ELS fibrils (Figs. 1A, 3D); one APR
184 overlapping CDR2 is disordered; and one APR overlapping CDR3 acquires variable
185 conformations in different amyloids[19,21]. The disulfide-forming residues C22 and C91 are
186 located in APRs in the structured regions near CDR1 and CDR3 (Fig. 1A), supporting the
187 importance of the disulfide-containing regions in amyloid formation[21,36].

188 The structured segments in AL-224L and AL55 amyloids are flattened but not planar and
189 are stacked in β-helix-like structures. In these structures, the rugged fibril ends expose
190 hydrophobic side chains I29, Y33, and Y37 from the major APR (Fig. 3E), which may help

recruit new protein molecules to the growing fibril end[26]. Residue segment N1-P14 protrudes from the plane of the CT-segment and interacts with strands across the central cleft that are one or two molecular layers up the fibril length, n to n+1 and n to n+2 (Fig. 3D). AL-9ELS amyloid also shows cross-layer interactions involving N1-P14 segment[21]. In all three amyloids, such cross-layer interactions sterically interlock different molecules contributing to fibril stability.

Mutations in CDR3 alter the CT-segment conformation affecting ligand binding

Mutations in the ordered segments of λ6-LC amyloids, which include CDR1 and CDR3, probably contribute to their structural differences (Fig. 5), while mutations in disordered segments such as the CDR2-containing linker probably influence the amyloid formation kinetics but not necessarily the ordered structure[22]. Amino acid sequence in CDR3 of λ6-LCs is particularly variable[6,7]. Compared to AL-224L, AL55 residues 96-101 from CDR3 differ in three substitutions and one insertion, while CDR3 residues in AL-9ELS differ in four substitutions, resulting in different CT-tail conformations. Importantly, in AL-224L amyloid, the CT-tail extends along the NT-segment exposing the side chains of Y90, Q92, and Y94 (Fig. 4A). However, in AL55 and AL-9ELS amyloids, the CT-tail folds back on the structured CT-segment and occludes these side chains (Figs. 4B, 5B,C).

The Y90 and Y94 rings form one of the most hydrophobic solvent-exposed surfaces on the AL-224L fibril (Fig. 3E), which is energetically unfavorable. Our cryo-EM map shows two large orphan densities, one near Y94 and Q92 side chains and another near Y90 and D88 side chains (Figs. 3C, 6A,B). To test the significance of these densities, we filtered the unmasked map to a high statistical significance threshold cutoff using false-discovery rate thresholding[37] (Supplemental Figure 1). The orphan densities were visible at a high threshold cutoff, excluding the possibility that they were noise and suggesting bound ligands. These ligands are absent from AL55 and AL-9ELS structures where this fibril surface is occluded by the CT-tail[21,26] (Fig. 5B,C). These results show how high sequence variability in CDR3 can translate into structural variability in the λ6-LC amyloid, leading to distinct patient-specific CT-tail conformations that critically influence amyloid-ligand binding.

AL-224L shows orphan density in a hydrophilic pore near an acidic-rich segment

Uncompensated charged segments in amyloids are highly energetically unfavorable due to a strong repulsion within and between molecular layers[38,39]. Conflicting interatomic forces in such segments can generate structurally frustrated regions with variable conformations[39]. LCs feature a highly charged conserved residue segment 84-88 (EDEAD in AL-224L and AL55, EDEAE in AL-9ELS). In the native LC structure, this segment is stabilized by an extensive network of salt bridges and hydrogen bonds (Fig. 1C). In λ6-LC amyloids, the acidic segment is located at the fibril surface forming a part of a variable hydrophilic pore (Fig. 5). In AL-224L amyloid this pore is enlarged and the EDEAD segment shows reduced local resolution indicating structural frustration (Fig. 2C).

Mutations in and near the pore probably contribute to differences in its structure. These differences between AL-224L and AL55 include R24G, G27A, and Q82K substitutions. In the narrow pore of AL55, the Y89 ring packs against G24 (Fig. 4B), but in AL-224L amyloid, the Y89 side chain orients towards the C22-C91 disulfide and forms a cation-π interaction with R24 (Fig. 4A). In AL-9ELS amyloid, R24 also interacts with Y89[21]. Notably, Y89 is highly conserved in λ6-LCs[11]. Therefore, R24G substitution alters the conformation of the highly conserved Y89 residue in the pore.

In AL55 and AL-9ELS amyloids the charges within the acidic-rich segment are partially balanced by the K82-E84 salt bridge; additional charge-charge interactions stabilize the acidic-rich segment in AL-9ELS (Fig. 5C). However, in AL-224L amyloid the K82Q substitution eliminates the sole stabilizing salt bridge thus increasing the charge imbalance at the acidic-reach segment (Fig. 4C), destabilizing the local backbone conformation (Fig. 2C), and contributing to the pore enlargement.

The cryo-EM map of AL-224L shows a strong orphan density in the pore near the side chains of R24, A87, and D85 (Figs. 3C, 6A-C). This density is well above the noise level based on the false-discovery rate map thresholding (Supplemental Fig. 1). The cryo-EM study of AL-9ELS also reports an orphan density in the pore near R24 and Y89 side chains[21]. In contrast, AL55 (which contains G24 instead of the bulky R24) shows no orphan density in the pore (Fig. 6D), suggesting that this density is associated with R24 but not G24 λ6-LC variants.

The orphan density in the hydrophilic pore of AL-224L amyloid likely represents a small water-soluble molecule that interacts via its acidic and hydrophobic moieties with R24 and A87, respectively. One possibility is acetate, an abundant tissue metabolite whose cardiac uptake increases in heart failure[40], which was the cause of death of patient AL-224. Analysis of fibril tissue extracts using an ELISA-based assay detected short-chain fatty acids (Table S4 and Fig. S6) confirming them as potential candidates for binding amyloid in tissues. Figure 6C illustrates how an acetate molecule can fit in the orphan density in the pore of AL-224L amyloid.

Registry shifts and backbone flipping in amyloid helps accommodate AL mutations

Compared to AL55, the wider pore in AL-224L amyloid is facilitated by a shift in the backbone registry of the steric zippers between the CT- and NT-segments (Fig. 4E,F). This registry shift propagates from the EDEAD segment towards the CDR2-containing linker encompassing a 30-residue segment 59-88. For example, in AL-224L the W36 side chain packs between the D61 and F63 side chains, yet in AL55 the W36 side chain packs against S69 (Fig. 4E,F). To accommodate such a 7-residue registry shift, the backbone in segment 69-74 is flipped in AL-224L relative to AL55, inverting the side chain orientation in this segment. Registry shifts with the backbone flipping are also seen in other structured residue segments including 8-11, 24-29, 69-74, and 81-83 (Fig. 4E,F). As a result, most residues pack differently in the X-Y plane of AL-224L and AL55 amyloids, yet the overall amyloid fold is largely preserved.

The AL-9ELS structure also shows registry shifts with backbone flipping. For example, segment 32-40, which packs antiparallel to segment 61-70 with one-residue registry shift

between AL-9ELS and AL-224L amyloids, shows an opposite side chain orientation in AL-9ELS compared to both AL-224L and AL55 amyloids (Fig. 5). These findings suggest that registry shifts and associated backbone flipping is a plausible general mechanism enabling amyloids adapt to mutations while largely preserving the amyloid fold (Fig. 7).

DISCUSSION

λ6-LC amyloids have shared structural features

We determined the single-filament structure of AL-224L cardiac amyloid at 2.92 Å resolution and compared it with the available amyloid structures of two other cardiac λ6-LCs, AL55 (4.0 Å resolution) and AL-9ELS (3.0 Å resolution). Despite 14 amino acid differences between AL-224L and AL55, these two amyloids have surprisingly similar overall folds (Fig. 4), while all three amyloids share key structural features (Fig. 5). These features include a structured fibril core comprised of antiparallel NT- and CT-segments connected by a disordered CDR2-containing linker. In λ1-LC and λ3-LC amyloids the CDR2-containing linker can be either ordered or disordered[13,23]. Importantly, in all LC amyloids NT- and CT-segments are linked by the conserved internal disulfide that maintains their antiparallel orientation providing a major constraint for amyloid formation and structure[13,21,23,25]. Furthermore, in λ6-LC amyloids the planar part of the CT-segment partially encircles the fibril surface, while the non-planar NT-segment forms cross-layer interactions. Lastly, the amyloid structure adjacent to the C22-C91 disulfide contains a variable pore; the pore is lined by mostly hydrophilic residues including the acidic-rich segment 84-88 (Fig. 4C,D), while the Y89 side chain packs against G24/R24 in the pore (Figs. 4A,B). Since in λ6-LCs residues 85-91 are highly conserved while residue 24 is typically either G or R[7,11], these structural features probably extend to other λ6-LC amyloids.

The observed structural similarities between the λ6-LC amyloids are facilitated, in part, by the registry shifts with backbone flipping in steric zippers (Figs. 4E,F, 7). Importantly, we were able to attribute the structural differences between amyloids to LC mutations, providing clear insights into the role of patient-specific AL mutations in amyloid polymorphism and ligand binding.

Germline λ6-LC is compatible with the amyloid folds in tissue-derived fibrils

The fibril-forming V_L domain in λ6-LCs is encoded by the germline gene *IGLV6-57* [10,11]. We propose that the hypothetical protein with the germline amino acid sequence can be accommodated in the structure of AL-224L and/or other tissue-derived amyloids (Fig. 1A). The germline-encoded residue V18 (I in AL-224L, L in AL55, and V in AL-9ELS) can be readily accommodated instead of I18 of AL-224L in the structured NT-segment in the hydrophobic amyloid core. The germline-encoded S44 (A in AL-224L, AL55, and AL-9ELS) can also be accommodated in the flexible CDR2-containing segment. Furthermore, the germline-encoded residue K82 (Q in AL-224L, K in AL55 and AL-9ELS) forms a stabilizing salt bridge with E84 in AL55 and AL-9ELS amyloids (Figs. 4D, 5B,C)[21,26]. Lastly, germline mutations in positions 99-101 of CDR3 are very different in AL-224L, AL55, and AL-9ELS (Fig. 1A) and probably influence the variable CT-tail conformation at the periphery of the

318 amyloid structure (Fig. 5). This analysis suggests that the amyloid folds observed in AL-
319 224L, AL55, and AL-9ELS are compatible with the germline LC, suggesting that aspects
320 of these folds are probably shared by other λ6-LC amyloids.

321 The amyloid structure of AL-9ELS differs significantly from those of AL-224L and AL55.
322 The major difference involves residue segment 1-14 that forms cross-layer interactions in
323 all three amyloids. In AL-224L and AL55 amyloids, residues 1-14 are centered in the snail
324 shell-shaped core (Fig. 5A,B), yet in AL-9ELS these residues wrap around the structural
325 periphery (Fig. 5C)[21]. Since residues 1-14 are identical in the three λ6-LCs (Fig. 1), their
326 conformational differences must reflect mutations located elsewhere. The likely
327 candidates include residues 18 and 32 in the middle of the snail shell-shaped NT-segment
328 (which harbors segment 1-7 in AL-224L and AL55 amyloids) and residues 95, 96, 99 and
329 100 in the CT-tail (which interacts with residues 1-14 in AL-9ELS amyloid) (Fig. 5). This
330 comparison illustrates how the combined effects of several AL mutations define the
331 amyloid conformation in a mutation-free segment.

332

333 **Low predicted stability of λ6-LC amyloid fibrils may promote pathology**

334 Prior biophysical studies of the natively folded recombinant human λ6-LCs did not show
335 reduced thermodynamic stability of AL-224L compared to non-amyloidogenic controls but
336 revealed subtle differences in local stability and proteolytic processing, which were
337 relevant to fibrillogenesis[19]. In the current study, we assessed the amyloid fibril stability.
338 PDBePISA software[41] was used to calculate free energy change upon exposure of one
339 fibril layer to solvent for AL-224L and AL55 amyloids, as well as for the hypothetical
340 germline λ6-LC sequence placed in these fibril structures.

341 AL-224L has slightly weaker solvation energy than AL55, indicating that it is slightly less
342 stable than AL55 (Table S3). Structures of AL-224L or AL55 amyloids containing the
343 hypothetical protein with the germline λ6-LC sequence showed comparable solvation
344 energies as tissue-derived AL-224L and AL55, indicating comparable stabilities (Table S3).
345 These calculations support our hypothesis that the germline λ6-LC sequence is
346 compatible with amyloid structures of the tissue-derived fibrils.

347 Next, we computed solvation energies for all other available LC amyloid structures using
348 PDBePISA. AL-224L and AL55 amyloids has lower solvation energies than λ1-LC and λ3-
349 LC amyloids (Table S3). The Saelices team also reported lower solvation energies for
350 AL55 and AL-9ELS compared to λ1-LC and λ3-LC amyloids[21]. These results suggest that,
351 compared to other amyloids from the λ-LC family, λ6-LC fibrils are relatively unstable and
352 can be fragmented more easily, potentially facilitating amyloid proliferation by seeding and
353 enhancing amyloid cytotoxicity[42].

354

355 **Role of registry shifts with backbone flipping in amyloid structures**

356 Comparison of AL-224L, AL55, and AL-9ELS amyloid structures revealed a shift in the
357 steric zipper registry with the backbone flipping in several well-ordered segments (Figs.
358 4E,F, 5). We posit that such amyloid-specific structural changes provide a general
359 mechanism for adapting the fibril core to protein mutations, post-translational

360 modifications, and structurally frustrated regions that are often interspersed with β-strands
361 in amyloids[39]. Registry shifts and backbone flipping in steric zippers help explain why the
362 risk of amyloid formation increases for proteins containing low-complexity domains and
363 amino acid repeats, such as poly-Q motif in huntingtin or tandem repeats in bacterial
364 amyloids[43–45]. Such repeating units can facilitate formation of steric zippers differing in the
365 backbone registry and side chain orientation to generate energetically equivalent but
366 conformationally distinct fibril polymorphs of the same or closely related proteins[46].
367

368 **A conserved acidic-rich segment is a potential gatekeeper in LC amyloid formation**

369 Unbalanced charges in amyloids are highly energetically unfavorable due to a strong
370 repulsion among molecular layers of parallel in-registry cross-β-sheets[38,39]. LCs contain a
371 conserved residue segment 85-91[11] that overlaps the acidic-rich segment 84-88, EDEAD.
372 We hypothesize that this acidic segment, which forms stabilizing interactions in the native
373 structure (Fig. 1C) but destabilizes the local structure in amyloid (Fig. 2C), acts as a
374 gatekeeper protecting LCs from amyloid formation. However, AL mutations can balance
375 the charge on this acidic segment to promote fibrillogenesis. Examples include K83 that
376 forms a K83-D85 salt bridge in AL-9ELS amyloid (Fig. 5C). Ligand binding at nearby sites,
377 such as the internal site near A87 and the external site near D88 and Y90 in AL-224L (Fig.
378 6), can also stabilize the acidic-rich segment 84-88 in amyloid and thereby promote
379 fibrillogenesis.

380

381 **R24 but not G24 variant is associated with ligand binding in amyloid pore**

382 Residue 24 is a site of an AL-associated polymorphism in λ6-LCs. R24 is the major variant
383 found in the germline, AL-224L, and AL-9EL LCs[47]. Compared to R24, G24, the second-
384 major variant found in AL55, is overrepresented in amyloidosis and is considered more
385 amyloidogenic[11]. Stabilizing electrostatic interactions involving R24 in the native LC
386 structure were proposed to counteract amyloid formation[47], but the effects of R24G
387 substitution on the amyloid structure and stability were unknown. Cryo-EM structures of
388 AL-224L, AL-9ELS, and AL55 amyloids show that G24 replacement with R24 induces local
389 structural changes in the hydrophilic pore including the pore enlargement (Figs. 5) likely
390 contributing to reduced amyloidogenicity of the R24 variant. Moreover, the orphan density
391 seen in amyloids near R24 in AL-224L and AL-9ELS, but not near G24 in AL55, represents
392 a bound ligand such as acetate (Fig. 6C). Ligand binding in an internal amyloid pore
393 probably occurs during fibril formation and may critically influence fibrillogenesis,
394 suggesting the direct involvement of residue 24 in this process.

395

396 **External ligand binding sites in AL-224L fibrils may harbor collagen triple helices**

397 The cryo-EM map of AL-224L shows two orphan densities, one near residues Y94 and
398 Q92 and another near Y90 and D88 (Fig. 6A,E). Mixed hydrophilic/hydrophobic
399 coordinating residues and the ~18 Å center-to-center separation between these densities
400 suggest that they potentially represent collagen triple helices (diameter 15 Å) and/or
401 apolipoprotein α-helices (diameter 11-13 Å) bound laterally along the fibril spine, as

402 previously reported for ColVI[13] and apoE[48]. In the current study, LC-MS/MS of the fibril
403 tissue extracts detected three chains of ColVI as well as apoE and apoA-IV co-purified
404 with fibrils (Table S2). The orphan density coordinated by Q92 and Y94 appears hollow in
405 the x-y plane (Fig. 6A) consistent with a triple helix. To test this hypothesis, we used
406 pyDock software[49] for rigid body docking of a canonical collagen triple helix to the AL-224L
407 fibril structure. As a model we used the crystal structure of a 30-residue collagen-like
408 peptide containing consensus sequence repeats Pro-Hyp-Gly (PDB ID: 1CAG)[50]. The top
409 two docking poses show triple helices bound along the Y90 and Y94 side chain amyloid
410 arrays (Fig. 6E,F). These docking poses closely superimpose the two orphan densities in
411 the EM map of AL-224L (Fig. 6E). Therefore, these densities likely represent collagen triple
412 helices bound along the fibril surface. The aromatic rings of amyloid stack against the
413 pyrrolidine rings of collagen. We hypothesize that similar interactions mediate longitudinal
414 binding of ColVI to λ3-AL59 cardiac amyloid[13]; in fact, orphan densities seen in the cryo-
415 EM map of AL59 amyloid near the exposed arrays of Y48 and Y35[13] overlap the top
416 docking poses of the collagen triple helix and hence may represent bound ColVI.

417 Direct interactions between collagen and aromatic residues have been reported for
418 globular proteins[51] including proteins featuring an immunoglobulin fold[52,53] such as an
419 amyloidogenic LC[54]. Our docking results suggest that ring-stacking interactions also
420 mediate collagen binding to amyloids along the fibril spine. Such a longitudinal binding is
421 expected to influence mechanical and biological properties of amyloid fibrils including
422 amyloid nucleation, growth, fragmentation, interactions with cells including phagocytosis,
423 and the uptake of diagnostic dyes[13,55,56]. Future studies will identify additional details of
424 such amyloid-ligand interactions and their roles in vivo.

425

426 **Acknowledgements** The authors are grateful to Dr. Esther Bullitt, the director of the
427 Boston University Cryo-EM Core Facility where the data was collected, to Dr. Luca
428 Broggini at the University of Pavia for invaluable advice on the cryo-EM structural analysis
429 of amyloids, and to Mei Chen and Steven Kolakowski at the Harvard Center for Mass
430 Spectrometry for their assistance with the proteomics analyses. We gratefully
431 acknowledge the patient's family for providing tissue samples for amyloid research.

432 **Funding**: This research was supported by the National Institute of General Medical
433 Sciences grants S10OD032253, GM135158, and GM067260**;** the Boston University
434 Amyloid Research Fund; Wildflower Foundation Fund; Fondo Italiano per la Scienza (FIS
435 2021) FIS00001548; Cariplo–Telethon grant 2022-0578; and PNRR grant ID MUR:
436 CN00000041.

437 **Competing interests** The authors declare no competing interests.

438 **Author contributions**

439 C.W.H. prepared the cryo-EM grids, collected cryo-EM data, performed data processing,
440 map interpretation, model building and refinement, and prepared graphics.

441 T.P. initiated the study, oversaw fibril extraction, LC-MS/MS analysis and immuno-EM,
442 interpreted the results, prepared graphics and contributed to draft writing.

B.S. performed fibril extraction, SDS-PAGE and western blotting, prepared samples for LC-MS/MS, contributed to immuno-EM, and prepared graphics.

S.J. performed biochemical assays, calculated solvation energies, performed molecular docking, and contributed to data analysis and interpretation.

N.H. prepared graphics and contributed to structural interpretation.

S.W. optimized sample preparations.

H.C. performed immuno-EM of the tissues and fibrils.

V.S. contributed to the overall study administration and funding.

F.L. oversaw fibril extraction, performed LC-MS/MS analysis and interpretation, and contributed graphics, draft writing, and funding.

O.G. administered the project, interpreted the results, wrote the first draft, and contributed to funding. C.W.H. and O.G. wrote the paper with input from all authors.

Data availability The AL-224L amino acid sequence has been deposited to the AL-base, and the gene sequence, *AL3IGLV6-57*01-IGLJ2*02-IGLC2*02* has been deposited in the GenBank (accession number KY432418). The cryo-EM model and map data have been deposited to the Protein Data Bank (PDB ID: 9OKA, EMDB code 70557). Raw cryo-EM movies have been deposited to the Electron Microscopy Public Image Archive (accession code EMPIAR-12815). The LC-MS/MS proteomics data have been deposited to the ProteomeXchange Consortium via the PRIDE partner repository (dataset identifiers PXD064296).

TABLES

Parameter	**Data Collection**
Magnification (X)	130,000
Voltage (kV)	200
Electron exposure (e^-/Å^2)	40
Dose rate (e^-/px/s)	10.82
Defocus range (μM)	-0.8 to -2.5
Pixel size (Å)	0.900
Camera	Falcon 4i
Energy Filter slit width (eV)	10
Micrographs (#)	10,309
	Data Processing
Box size (px)	400
Segment separation distance (Å)	45
Initial uncleaned segment stack (#)	421,024
Helical rise (Å)	4.86
Helical twist (°)	1.20
Particle duplication symmetry	C1
Final segments (#)	214,100
Map resolution at 0.143 FSC cutoff (Å)	2.92
	Model Building and Validation
Non-hydrogen atoms (#)	3,335
Subunits	5
CC mask	0.75
Bond length RMSD (Å)	0.002
Bond angles RMSD (°)	0.602
Clash score	7.82
Ramachandran Outliers (%)	0
Ramachandran Allowed (%)	6.02
Ramachandran Favored (%)	93.98
Rotamer Outliers (%)	0
C-beta outliers (%)	0
MolProbity score	1.83

Table 1 Cryo-EM statistics and validation metrics. Table of details related the cryo-EM structure of AL-224L amyloid. The details include parameters for data collection, data processing, model building, and validation.

FIGURES

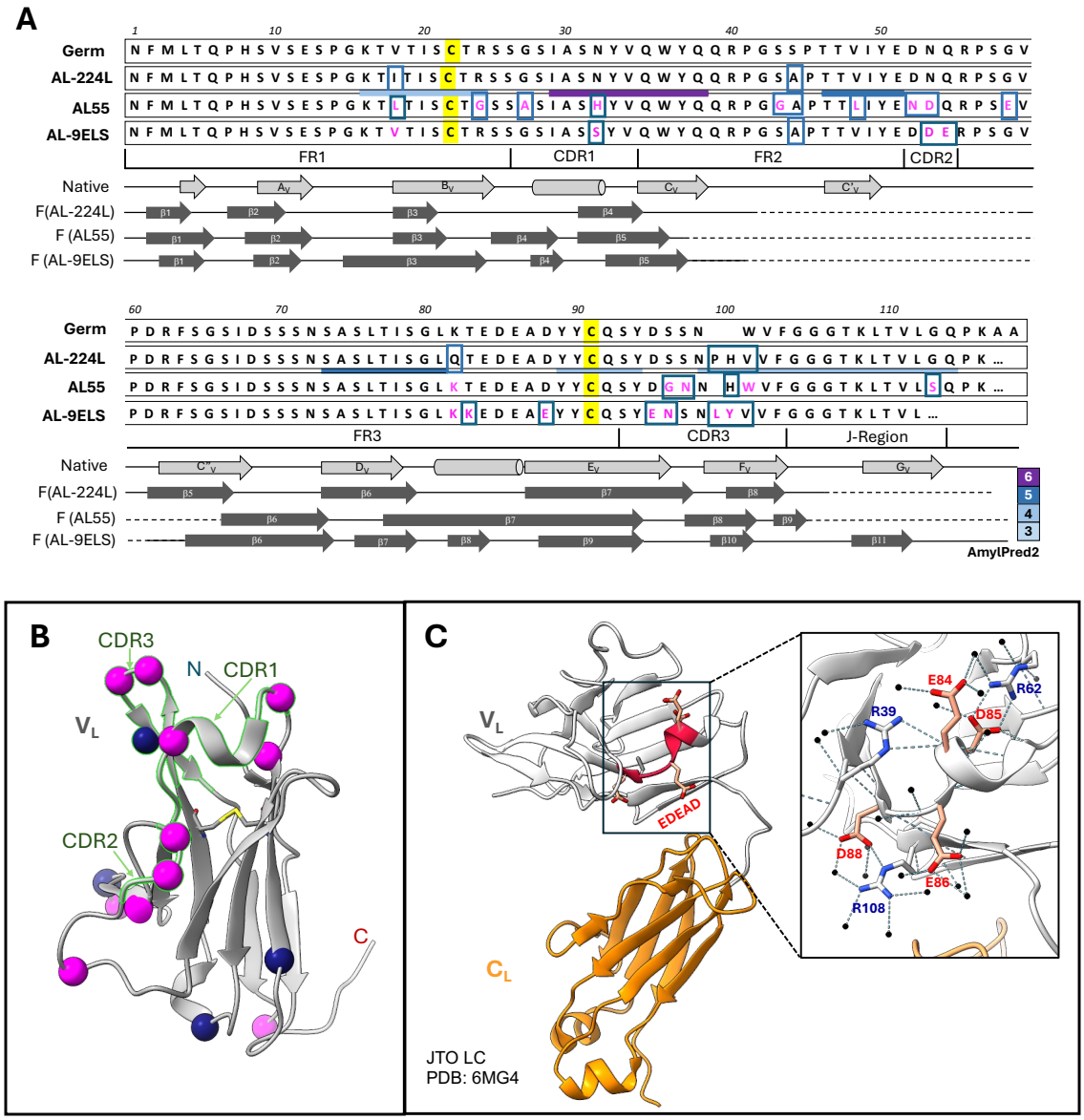

Figure 1. Structural properties of λ6-LCs explored in this study.
A, Top to bottom: Amino acid sequences of the λ6 germline, AL-224L, AL55, and AL-9ELS V_L domains (consecutive residue numbering). AL55 and AL-9ELS residue differences compared to AL-224L (magenta). AL-224L, AL55, and AL-9ELS residue differences compared to germline LC (boxed). Amyloid-promoting regions in AL-224L (horizontal bars) are colored according to the consensus number predicted using AmylPred2[35]. Framework regions (FR), complementarity determining regions (CDRs), the J-region, and the proximal end of C_L domain are marked. Linear diagrams show secondary structures of λ6-LCs including β-strands (arrows), α-helices (cylinders), loops/turns (solid lines), and disordered regions (broken lines). "Native" denotes the native fold according to the x-ray crystal structure of a related λ6-LC protein, JTO (PDB ID: 6MG4); "F" denotes amyloid fibril structures of AL-224L (PDB ID: 9OKA), AL55 (PDB ID: 6HUD), and AL-9ELS (PDB ID: 9ELS) determined by cryo-EM.
B, Native structure of V_L domain (PDB ID: 6MGT). CDRs are highlighted. Spheres mark residues differentiating AL55 from AL-224L (magenta) and AL-224L from the germline LC (blue).
C, Native structure of full-length LC. The acidic-rich segment 84-88 (red). Zoomed-in view of the boxed area shows salt bridges and hydrogen bonds stabilizing the charges in this acidic segment.

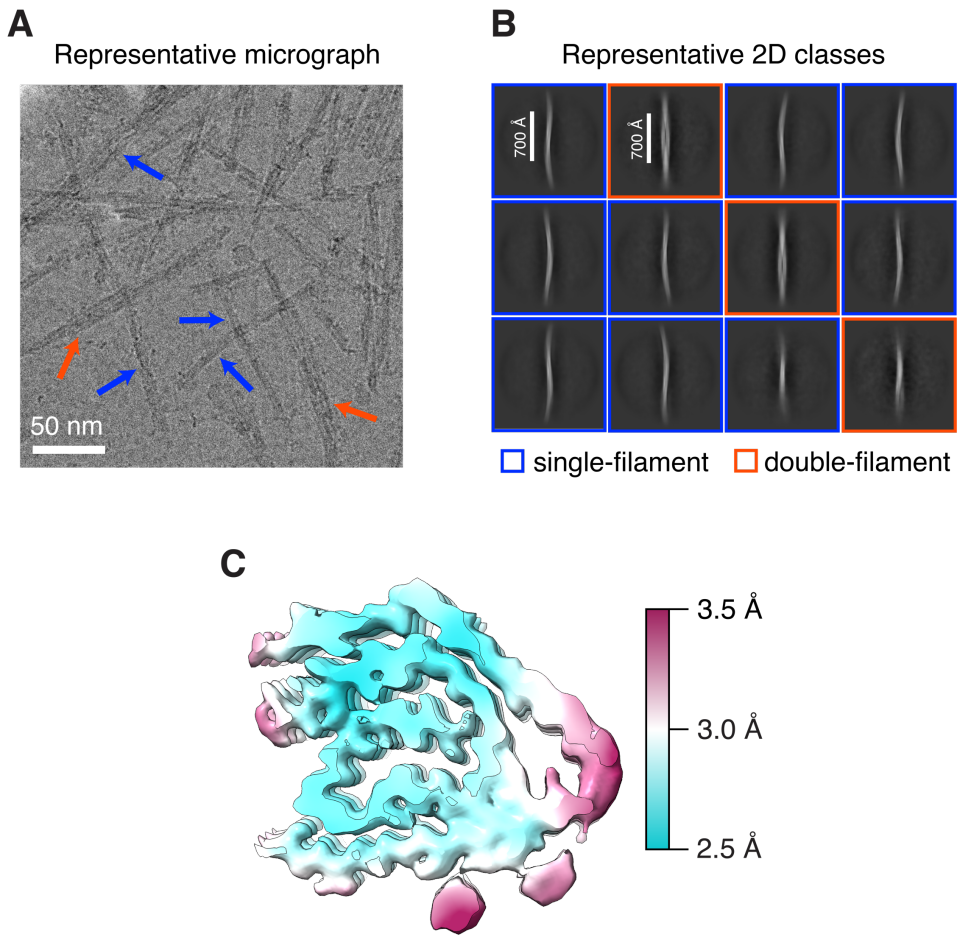

Figure 2. Amyloid fibril polymorphs and local resolution of the single-filament AL-224L structure.
A, Representative cropped micrograph shows single (blue arrows) and double filaments (red arrows).
B, Representative 2D classes at a box size 1800 px (1620 Å) show an approximate crossover distance of 700 Å for both single and double filaments.
C, Cross-section of one molecular layer of the cryo-EM density map colored by local resolution.

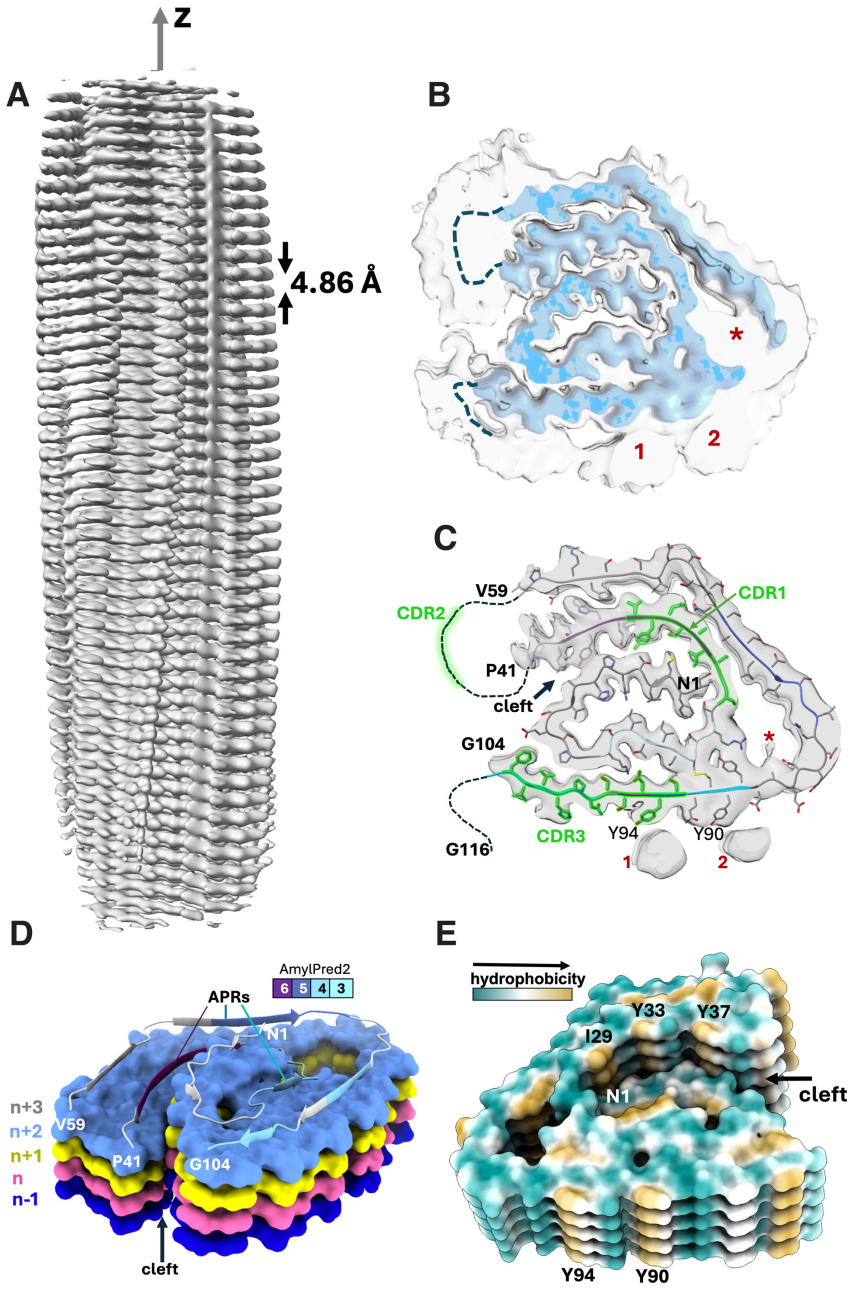

Figure 3. Structural overview of the AL-224L single-filament amyloid polymorph.
A, Sharpened cryo-EM map (2.9 Å) of AL-224L amyloid (side view).
B, EM map (top view) showing well-ordered fibril core (blue, contouring threshold 0.0994) and lower-order regions (gray, threshold 0.0325). Disordered segments 42-58 and 105-116 (dashed lines).
C, Cross-section of one fibril layer superimposed on the cryo-EM map. Stick model shows ordered segments N1-P41 (NT-segment) and V59-G104 (CT-segment). CDRs are colored in green and orphan densities are labeled as 1, 2, and *.
D, A stack of molecular layers shows n to n+1 and n to n+2 interlayer contacts across the central cleft (top view). APRs in the top layer are color-coded from least amyloidogenic (cyan) to most amyloidogenic (purple), as in Fig. 1A.
E, Surface representation of five molecular layers colored according to side chain hydrophobicity (bottom view).

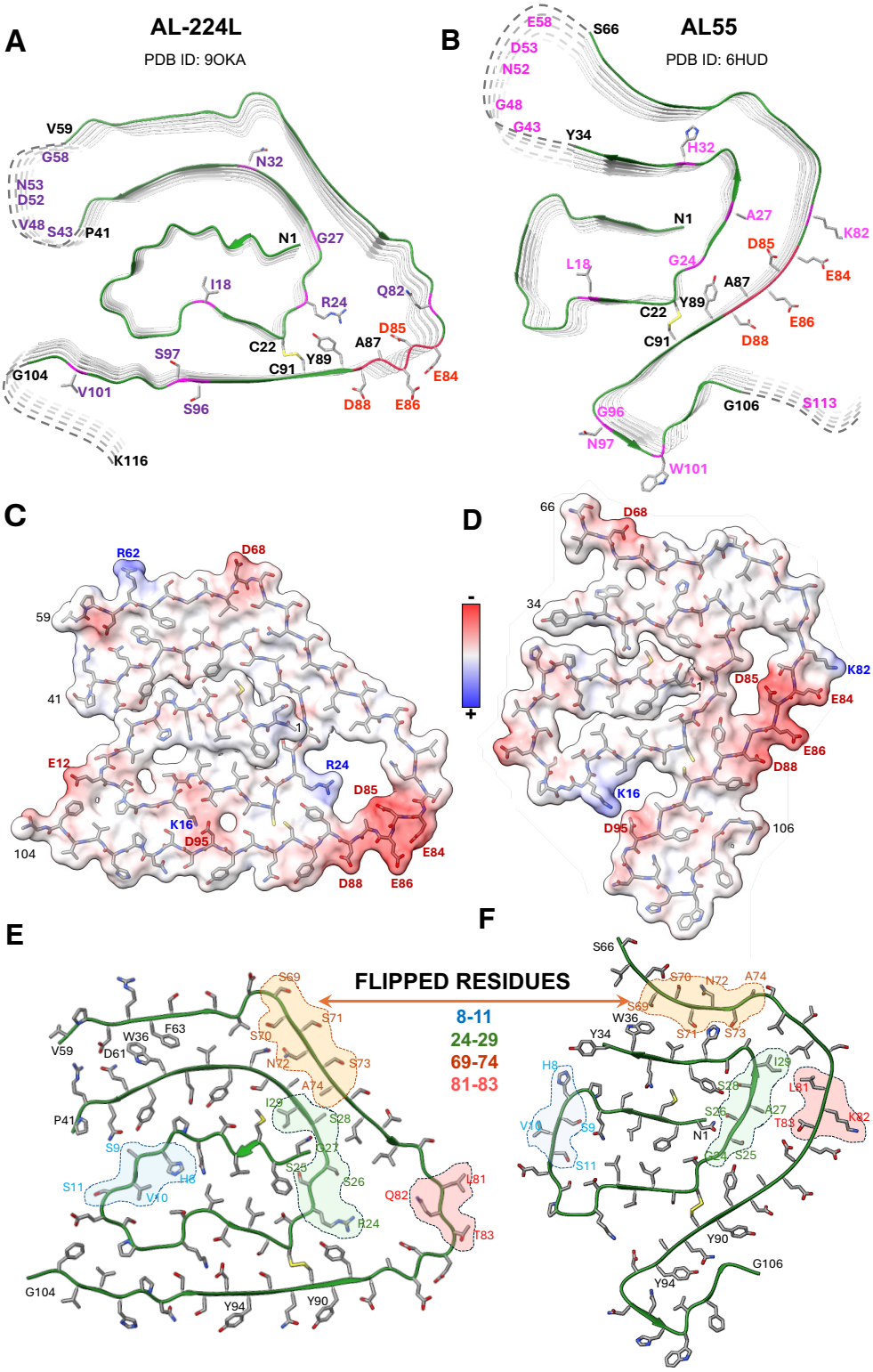

Figure 4. Comparison of AL-224L and AL55 fibril structures.
A, B, Cross-sectional top views show proteins' backbone in five molecular layers. Residues that differ in AL-224L (violet) and AL55 (magenta), residues in the acidic-rich segment (red), and other residues mentioned in the manuscript (black) are shown.
C, D, Space-filling model of one fibril layer colored according to coulombic potential.
E, F, Regions showing opposite side chain orientation (backbone flipping) in AL-224L vs. AL55 amyloids.

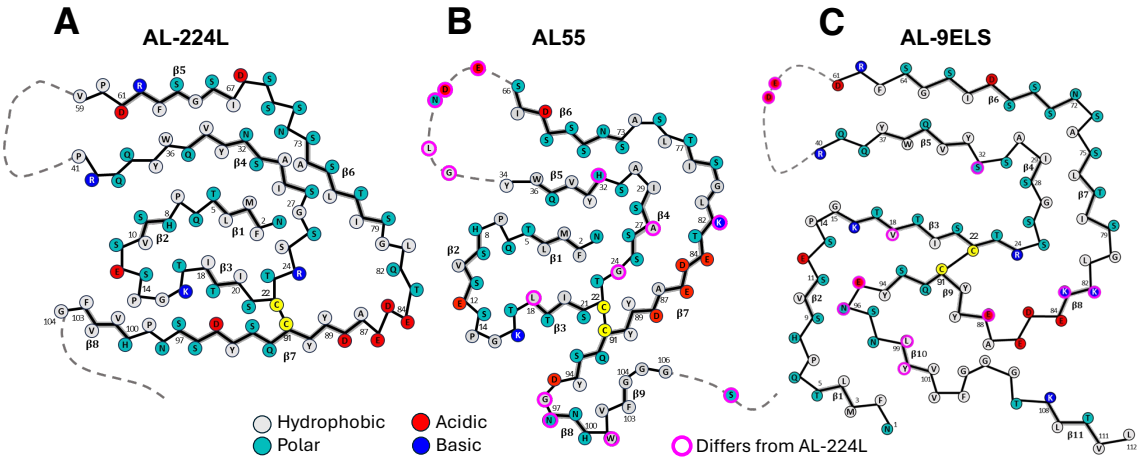

Figure 5. Three available λ6-LC cardiac amyloid structures.
Schematic diagram showing the polypeptide sequence and fold in the fibril core of AL-224L (PDB ID: 9OKA) **(A)**, AL-55 (PDB ID: 6HUD) **(B)**, and AL-9ELS (PDB ID: 9ELS) **(C)**. β-strands shown as thick lines; disordered regions shown as dashed lines.

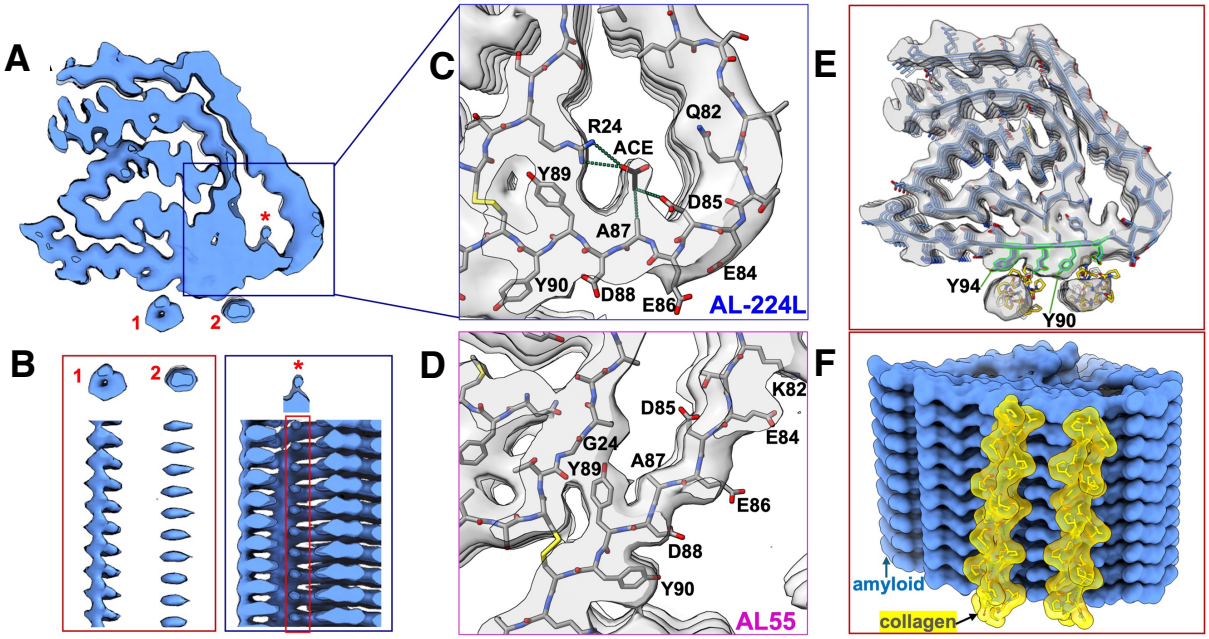

Figure 6. Orphan densities in the cryo-EM map of AL-224L amyloid.
A, Sharpened cryo-EM density map shows one fibril layer (top view) with orphan densities at external (1, 2) and internal (*) sites.
B, Side views show orphan densities in the maps at a threshold of 0.0781 (1, 2) or 0.0567 (*).
C, Zoomed-in view of the EM map and model of the hydrophilic pore in AL-224L shows acetate (ACE) molecule manually fitted in the extra density. Dotted lines show acetate-protein contacts within 4 Å.
D, A view similar to panel C of the amyloid pore in AL55.
E, Cryo-EM map and model of AL-224L show two top docking poses of collagen triple helix (PDB ID: 1CAG).
F, Side view of the space-filling model shows top two docking poses of collagen (yellow) to AL-224L amyloid (blue).

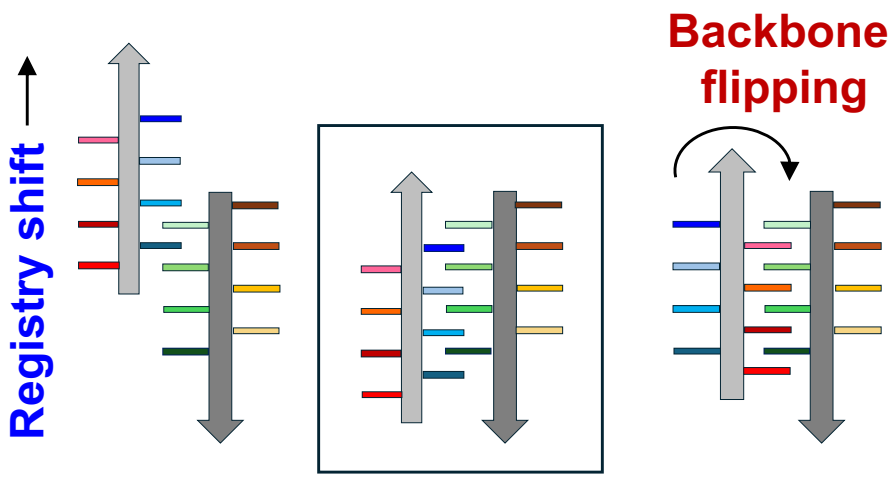

Figure 7. Schematic diagram illustrating registry shifts and backbone flipping in a steric zipper. A steric zipper before registry shift and backbone flipping (middle). A steric zipper after registry shift (left). A steric zipper after backbone flipping (right). b-strands are shown as gray arrows; side chains are shown as colored bars.

534 **References**

535 1. Merlini, G. *et al.* Systemic immunoglobulin light chain amyloidosis. *Nat Rev Dis Primers*
536 **4**, 38 (2018).

537 2. Gertz, M. A. & Dispenzieri, A. Systemic Amyloidosis Recognition, Prognosis, and
538 Therapy: A Systematic Review. *JAMA* **324**, 79–89 (2020).

539 3. Sanchorawala, V. Systemic Light Chain Amyloidosis. *N Engl J Med* **390**, 2295–2307
540 (2024).

541 4. Merlini, G. AL amyloidosis: from molecular mechanisms to targeted therapies.
542 *Hematology Am Soc Hematol Educ Program* **2017**, 1–12 (2017).

543 5. Morgan, G. J., Buxbaum, J. N. & Kelly, J. W. Light Chain Stabilization: A Therapeutic
544 Approach to Ameliorate AL Amyloidosis. *Hemato* **2**, 645–659 (2021).

545 6. Bellotti, V., Mangione, P. & Merlini, G. Review: immunoglobulin light chain amyloidosis--
546 the archetype of structural and pathogenic variability. *J Struct Biol* **130**, 280–289 (2000).

547 7. Del Pozo-Yauner, L. *et al.* Role of the mechanisms for antibody repertoire diversification
548 in monoclonal light chain deposition disorders: when a friend becomes foe. *Front*
549 *Immunol* **14**, 1203425 (2023).

550 8. Absmeier, R. M., Rottenaicher, G. J., Svilenov, H. L., Kazman, P. & Buchner, J. Antibodies
551 gone bad - the molecular mechanism of light chain amyloidosis. *FEBS J* **290**, 1398–1419
552 (2023).

553 9. Haupt, C. The AL Amyloid Fibril: Looking for a Link between Fibril Formation and
554 Structure. *Hemato* **2**, 505–514 (2021).

555 10. Bodi, K. *et al.* AL-Base: a visual platform analysis tool for the study of amyloidogenic
556 immunoglobulin light chain sequences. *Amyloid* **16**, 1–8 (2009).

557 11. Morgan, G. J. *et al.* An updated AL-base reveals ranked enrichment of immunoglobulin
558 light chain variable genes in AL amyloidosis. *Amyloid* **32**, 129–138 (2025).

559 12. Lavatelli, F. *et al.* Mass spectrometry characterization of light chain fragmentation sites
560 in cardiac AL amyloidosis: insights into the timing of proteolysis. *J Biol Chem* **295**,
561 16572–16584 (2020).

562 13. Schulte, T. *et al.* Helical superstructures between amyloid and collagen in cardiac fibrils
563 from a patient with AL amyloidosis. *Nat Commun* **15**, 6359 (2024).

564 14. Brumshtein, B. *et al.* Inhibition by small-molecule ligands of formation of amyloid fibrils
565 of an immunoglobulin light chain variable domain. *Elife* **4**, e10935 (2015).

566 15. Blancas-Mejia, L. M. *et al.* Immunoglobulin light chain amyloid aggregation. *Chem*
567 *Commun (Camb)* **54**, 10664–10674 (2018).

568 16. Kazman, P. *et al.* Fatal amyloid formation in a patient's antibody light chain is caused by
569 a single point mutation. *Elife* **9**, e52300 (2020).

570 17. Peterle, D. *et al.* A Conservative Point Mutation in a Dynamic Antigen-binding Loop of
571 Human Immunoglobulin λ6 Light Chain Promotes Pathologic Amyloid Formation. *J Mol*
572 *Biol* **433**, 167310 (2021).

573 18. Radamaker, L. *et al.* Cryo-EM reveals structural breaks in a patient-derived amyloid fibril
574 from systemic AL amyloidosis. *Nat Commun* **12**, 875 (2021).

575 19. Klimtchuk, E. S. *et al.* Conformational Differences in the Light Chain Constant Domain
576 of Immunoglobulin G and Free Light Chain May Influence Proteolysis in AL Amyloidosis.
577 *J Mol Biol* **436**, 168837 (2024).

578 20. Paissoni, C. *et al.* A conformational fingerprint for amyloidogenic light chains. *Elife* **13**,
579 RP102002 (2025).

580 21. Cryo-EM reveals that cardiac IGLV6-derived AL fibrils can be polymorphic | bioRxiv.
581 https://www.biorxiv.org/content/10.1101/2024.12.04.626857v1.

582 22. Ulamec, S. M., Brockwell, D. J. & Radford, S. E. Looking Beyond the Core: The Role of
583 Flanking Regions in the Aggregation of Amyloidogenic Peptides and Proteins. *Front*
584 *Neurosci* **14**, 611285 (2020).

585 23. Karimi-Farsijani, S. *et al.* Light chain mutations contribute to defining the fibril
586 morphology in systemic AL amyloidosis. *Nat Commun* **15**, 5121 (2024).

587 24. Puri, S. *et al.* The Cryo-EM Structure of Renal Amyloid Fibril Suggests Structurally
588 Homogeneous Multiorgan Aggregation in AL Amyloidosis. *J Mol Biol* **435**, 168215 (2023).

589 25. Radamaker, L. *et al.* Cryo-EM structure of a light chain-derived amyloid fibril from a
590 patient with systemic AL amyloidosis. *Nat Commun* **10**, 1103 (2019).

591 26. Swuec, P. *et al.* Cryo-EM structure of cardiac amyloid fibrils from an immunoglobulin
592 light chain AL amyloidosis patient. *Nat Commun* **10**, 1269 (2019).

593 27. Tunyasuvunakool, K. *et al.* Highly accurate protein structure prediction for the human
594 proteome. *Nature* **596**, 590–596 (2021).

595 28. Klimtchuk, E. S. *et al.* The critical role of the constant region in thermal stability and
596 aggregation of amyloidogenic immunoglobulin light chain. *Biochemistry* **49**, 9848–9857
597 (2010).

598 29. Enqvist, S., Sletten, K. & Westermark, P. Fibril protein fragmentation pattern in systemic
599 AL-amyloidosis. *J Pathol* **219**, 473–480 (2009).

600 30. Scheres, S. H. W. Amyloid structure determination in RELION-3.1. *Acta Crystallogr D*
601 *Struct Biol* **76**, 94–101 (2020).

602 31. Hansen, K. H. *et al.* Structure of biofilm-forming functional amyloid PSMα1 from
603 Staphylococcus aureus. *Proc Natl Acad Sci U S A* **121**, e2406775121 (2024).

604 32. Bu, F., Dee, D. R. & Liu, B. Structural insight into Escherichia coli CsgA amyloid fibril
605 assembly. *mBio* **15**, e0041924 (2024).

606 33. Iadanza, M. G., Jackson, M. P., Hewitt, E. W., Ranson, N. A. & Radford, S. E. A new era for
607 understanding amyloid structures and disease. *Nat Rev Mol Cell Biol* **19**, 755–773
608 (2018).

609 34. Sawaya, M. R., Hughes, M. P., Rodriguez, J. A., Riek, R. & Eisenberg, D. S. The expanding
610 amyloid family: Structure, stability, function, and pathogenesis. *Cell* **184**, 4857–4873
611 (2021).

612 35. Tsolis, A. C., Papandreou, N. C., Iconomidou, V. A. & Hamodrakas, S. J. A consensus
613 method for the prediction of 'aggregation-prone' peptides in globular proteins. *PLoS*
614 *One* **8**, e54175 (2013).

615 36. Klimtchuk, E. S. *et al.* Role of complementarity-determining regions 1 and 3 in
616 pathologic amyloid formation by human immunoglobulin κ1 light chains. *Amyloid* **30**,
617 364–378 (2023).

618 37. Beckers, M., Jakobi, A. J. & Sachse, C. Thresholding of cryo-EM density maps by false
619 discovery rate control. *IUCrJ* **6**, 18–33 (2019).

620 38. Lewkowicz, E., Jayaraman, S. & Gursky, O. Protein Amyloid Cofactors: Charged Side-
621 Chain Arrays Meet Their Match? *Trends Biochem Sci* **46**, 626–629 (2021).

622 39. van der Kant, R., Louros, N., Schymkowitz, J. & Rousseau, F. Thermodynamic analysis of
623 amyloid fibril structures reveals a common framework for stability in amyloid
624 polymorphs. *Structure* **30**, 1178-1189.e3 (2022).

625 40. Palm, C. L., Nijholt, K. T., Bakker, B. M. & Westenbrink, B. D. Short-Chain Fatty Acids in
626 the Metabolism of Heart Failure - Rethinking the Fat Stigma. *Front Cardiovasc Med* **9**,
627 915102 (2022).

628 41. Krissinel, E. & Henrick, K. Inference of macromolecular assemblies from crystalline
629 state. *J Mol Biol* **372**, 774–797 (2007).

630 42. Xue, W.-F. *et al.* Fibril fragmentation enhances amyloid cytotoxicity. *J Biol Chem* **284**,
631 34272–34282 (2009).

632 43. Lee, M., Ghosh, U., Thurber, K. R., Kato, M. & Tycko, R. Molecular structure and
633 interactions within amyloid-like fibrils formed by a low-complexity protein sequence
634 from FUS. *Nat Commun* **11**, 5735 (2020).

635 44. Tayeb-Fligelman, E. *et al.* Low complexity domains of the nucleocapsid protein of SARS-
636 CoV-2 form amyloid fibrils. *Nat Commun* **14**, 2379 (2023).

637 45. Nowakowska, A. W., Wojciechowski, J. W., Szulc, N. & Kotulska, M. The role of tandem
638 repeats in bacterial functional amyloids. *J Struct Biol* **215**, 108002 (2023).

639 46. Louros, N. *et al.* Local structural preferences in shaping tau amyloid polymorphism. *Nat*
640 *Commun* **15**, 1028 (2024).

641 47. del Pozo Yauner, L. *et al.* Influence of the germline sequence on the thermodynamic
642 stability and fibrillogenicity of human lambda 6 light chains. *Proteins* **72**, 684–692
643 (2008).

644 48. Lewkowicz, E., Nakamura, M. N., Rynkiewicz, M. J. & Gursky, O. Molecular modeling of
645 apoE in complexes with Alzheimer's amyloid-β fibrils from human brain suggests a

646 structural basis for apolipoprotein co-deposition with amyloids. *Cell Mol Life Sci* **80**,
647 376 (2023).

648 49. Grosdidier, S., Pons, C., Solernou, A. & Fernández-Recio, J. Prediction and scoring of
649 docking poses with pyDock. *Proteins* **69**, 852–858 (2007).

650 50. Bella, J., Eaton, M., Brodsky, B. & Berman, H. M. Crystal and molecular structure of a
651 collagen-like peptide at 1.9 A resolution. *Science* **266**, 75–81 (1994).

652 51. Li, W. *et al*. The structural basis for the collagen processing by human
653 P3H1/CRTAP/PPIB ternary complex. *Nat Commun* **15**, 7844 (2024).

654 52. Liu, Q. *et al*. The Enterococcus faecalis MSCRAMM ACE binds its ligand by the Collagen
655 Hug model. *J Biol Chem* **282**, 19629–19637 (2007).

656 53. Hoop, C. L. *et al*. Collagen I Weakly Interacts with the β-Sheets of β2-Microglobulin and
657 Enhances Conformational Exchange To Induce Amyloid Formation. *J Am Chem Soc*
658 **142**, 1321–1331 (2020).

659 54. Harris, D. L., King, E., Ramsland, P. A. & Edmundson, A. B. Binding of nascent collagen
660 by amyloidogenic light chains and amyloid fibrillogenesis in monolayers of human
661 fibrocytes. *J Mol Recognit* **13**, 198–212 (2000).

662 55. Jackson, J. W. *et al*. Collagen inhibits phagocytosis of amyloid in vitro and in vivo and
663 may act as a 'don't eat me' signal. *Amyloid* **30**, 249–260 (2023).

664 56. Lewkowicz, E., Jayaraman, S. & Gursky, O. Molecular basis for non-invasive diagnostics
665 of cardiac amyloids using bone tracers. *Biomater Sci* **12**, 4275–4282 (2024).
666

667 **METHODS**

668 **Clinical data, sample collection and clinical characterization of patient AL-224**

669 The study was conducted in accordance with the Declaration of Helsinki. Informed consent
670 for the data and sample collection was obtained from the patient at presentation with the
671 approval of the Institutional Review Board at Boston Medical Center. Bone marrow
672 aspirate, clinical information, laboratory data, and post-mortem heart tissue were obtained
673 from the sample biorepository and patient database maintained by the Boston University
674 Amyloidosis Center.

675 Detailed clinical and laboratory characteristics of patient AL-224 are provided in Table S1
676 and in[19]. Briefly, a 63-year-old female with treatment naïve AL amyloidosis presented with
677 cardiac and soft tissue involvements; λ LC restriction; circulating clonal IgG and λ free LC
678 (FLC) on serum immunofixation electrophoresis; abnormal FLC κ/λ ratio; and λ FLC on
679 urine immunofixation electrophoresis. The abdominal fat aspirate and endomyocardial
680 and bone marrow biopsies were positive for amyloid by Congo red staining imaged using
681 light microscopy in bright and polarized light.

682 The amyloid fibril typing by either immunoelectron microscopy or mass spectrometry was
683 not available at the time of patient's evaluation. The patient passed away of cardiac arrest
684 one month after the initial evaluation. Post-mortem evaluation demonstrated interstitial
685 and vascular amyloid deposition in multiple organs, including the heart. The unfixed post-
686 mortem cardiac tissue was frozen at -80 °C; formalin-fixed paraffin-embedded cardiac
687 tissue block was made and used for further studies.

688 **Histological and immunoelectron microscopy analyses of cardiac tissue**

689 Post-mortem cardiac tissue was evaluated for amyloid by Congo red staining / light
690 microscopy. Amyloid typing in cardiac tissue was performed using immunogold electron
691 microscopy with antibodies directed against λ and κ LCs as previously described[57]. Briefly,
692 for primary antibodies we used polyclonal rabbit anti-human antibodies against λ and κ
693 LCs (Agilent Tech, Cat. #A019102-2 and #A019302-2). Secondary goat anti-rabbit IgG
694 antibody conjugated to 15 nm gold particles (Ted Pella, Cat. #15727) and goat anti-mouse
695 IgG antibody conjugated to 20 nm gold particles (Ted Pella, Cat. #15753) were used. The
696 micrographs were collected using a JEOL JEM1020 transmission electron microscope.

697

698 **Gene sequencing**

699 The *IGL* gene was cloned and sequenced from unselected bone marrow plasma cells as
700 previously described[58]. Once the *IGLV* gene was identified, nucleotide sequence errors
701 introduced by FR1 primers were corrected by additional PCR amplification with 5′ primer
702 for the *IGLV6-57* leader region and a 3′ universal *IGLC* primer. The light chain sequence,
703 AL-224L, was deposited in GenBank (accession number KY432418).

704 **Amyloid fibril extraction from autopsied cardiac tissue**

705 Fibrils were extracted from the tissue as previously described[26] using overnight tissue
706 digestion with C. histolyticum collagenase (5 mg/ml in a buffer containing 20 mM Tris, 140
707 mM NaCl, 2 mM $CaCl_2$, pH 8.0), followed by 15 cycles of homogenization in Tris EDTA
708 buffer (20 mM Tris, 140 mM NaCl, 10 mM EDTA, pH 8.0) to remove soluble proteins, and
709 by repeated homogenization of the remaining pellet in 1 ml ultrapure water. The fibril-
710 containing supernatants from the water homogenization cycles were retained. To evaluate
711 the protein yield, each 1 ml fraction was quantified using a Pierce BCA Protein Assay Kit
712 (Thermo Fisher Scientific). The cryo-EM and proteomic analyses were performed using
713 the supernatant from the third water-extraction cycle (water fraction 3), which was visibly
714 cloudy. 2D-PAGE and western blot analyses of amyloid fibril extract 2D SDS-PAGE was
715 performed under denaturing and reducing conditions as previously described[26]. Briefly,
716 proteins from water fraction 3 (200 µg) solubilized in the isoelectric focusing buffer (IEF)
717 were first separated on 11 cm strips with immobilized non-linear pH gradient 3–10 (Bio-
718 Rad) using a Bio-Rad Protean IEF cell, and then on 8–16% polyacrylamide gradient gels
719 (Criterion TGX gels, Bio-Rad). Gels were stained with GelCode Blue Stain Reagent
720 (Thermo Fisher Scientific) and imaged using an ImageQuant LAS 4000 (GE). Spots of
721 interest were excised and the proteins were identified by mass spectrometry as described
722 below. For western blotting, proteins were transferred overnight onto a PVDF membrane
723 (Millipore) using Criterion Blotter (Bio-Rad) and probed with a polyclonal rabbit anti-human
724 λ LCs antibody (Fortis Life Sciences) used at a concentration of 0.125 µg/ml.

725 **Proteomic analysis of fibril extracts by LC-MS/MS**

726 For proteomic analysis of the extracted fibrils from water fraction 3, 25 µg of proteins were
727 subjected to in-solution digestion with MS-grade trypsin (Thermo Fisher Scientific;
728 enzyme:protein ratio 1:20) overnight at 37 °C. For excised protein spots #15 and #16 from

729 the 2D SDS-PAGE, in-gel digestion was performed as described[26]. Samples were cleaned
730 up with Thermo SPE C18 tips and the LC-MS/MS analysis was conducted using Q
731 Exactive HF-X High Resolution Orbitrap (Thermo Fisher Scientific) coupled with Ultimate
732 3000 nanoLC (Thermo Fisher Scientific) at Harvard Center for Mass Spectrometry.
733 Peptides were trapped on a trapping cartridge (300 µm x 5 mm PepMap™ Neo C18 Trap
734 Cartridge, Thermo Fisher Scientific) prior to separation on an analytical column (µPAC,
735 C18 pillar surface, 50 cm bed, Thermo Fisher Scientific). Mobile phase system consisted
736 of water with 1% formic acid (A) and acetonitrile with 1% formic acid (B), using a gradient
737 elution for the total of 110 min (1-32% B over 80 min followed by 32-45% B over 20 min),
738 followed by washout with up to 95% B at a flow rate of 300 nl/min. The mass spectrometer
739 operated in positive mode and data dependent acquisition for all analyses. A full scan
740 ranging from 350 to 1400 m/z was performed with a mass resolution of 12×10^4. The top
741 three most intensive precursor ions from each scan were used for MS2 fragmentation with
742 normalized collision energy of 30 at a mass resolution of $3.0\text{x}10^4$. Data were processed
743 using the Proteome Discoverer software (Thermo Fisher Scientific) version 3.1, using a
744 human protein database downloaded in November 2024 from UNIPROT and augmented
745 with the AL-224L sequence. The following criteria were used for identification: cleavage
746 enzyme trypsin (semi-specific); cysteines carbamidomethylation (as a static modification);
747 and methionine oxidation and conversion of N-terminal glutamine into pyroglutamate (as
748 dynamic modifications).

749 **Short chain fatty acid (SCFA) quantification in fibril extracts**

750 Fibril extracts were tested for the presence of SCFA (1-6 carbons), which were quantified
751 using an ELISA kit (AFG Scientific, Cat. #EK700010) following manufacturer's protocols.
752 Homogenized and collagenase-treated cardiac tissue (220 mg) was extracted into ten 1 ml
753 fractions as described above. Fraction 3 was used for cryo-EM analysis and fractions 1 to
754 5 were used for SCFA measurements. Each fraction was diluted 1:5 in the assay buffer
755 and was assayed using 10 µl/well. The assay was performed in technical and biological
756 duplicates. SCFA concentrations were interpolated from the standard curve ($R^2 = 0.97$).
757 The results are reported in Figure S6.

758 **Assay Validation**: To evaluate the antibody selectivity for SCFA vs. non-esterified fatty
759 acids (NEFA) and potential interference from extracellular matrix components in tissue
760 extracts, the following validation experiments were performed. (i) Fractions 1-5 were
761 analyzed to assess the overall assay performance and the interference from NEFA; (ii)
762 Fraction 3 (Fr 3) was spiked with 12 or 24 μmol/l SCFA to test the signal recovery and
763 interference; (iii) 20 μmol/l SCFA was mixed with 20 μmol/l palmitic acid (a representative
764 NEFA) to probe antibody selectivity; (iv) combined spike tests were performed using Fr3
765 alone, Fr3 + 20 μmol/l SCFA, Fr3 + 20 μmol/l NEFA, and Fr3 + 20 μmol/l SCFA + 20 μmol/l
766 NEFA. The results, reported in Table S4, indicated minimal interference from tissue
767 components and no cross-reactivity with NEFAs, with high signal recovery ranging from
768 85 to 95%. These results confirm the specificity and robustness of the ELISA
769 measurements of SCFA in cardiac tissue extracts.

770 The endogenous SCFA concentration measured by ELISA in fraction 3 was
771 38.7 ± 1.2 μmol/l (or ~0.17 μmol/g tissue). Total protein concentration in fraction 3
772 measured by a colorimetric bicinchoninic acid assay was ~3 mg/ml. Assuming that most
773 of the protein in fraction 3 was the fibril-forming LC fragment 1-116, an approximate molar
774 ratio of LC to SCFA was 3:1. Assuming that SCFA had unit occupancy in the single-filament
775 structure (acetate in Figure 6C), LC to SCFA molar ratio in this structure was 1:1.

776 **Amyloid assay using thioflavin T fluorescence**

777 Amyloid content in tissue fractions 1-5 was assessed using thioflavin T (ThT), a diagnostic
778 dye that shows increased fluorescence upon binding to amyloid. Fractions 1-5 were
779 diluted 1:5 with Tris NaCl buffer, pH 7.92, and 10 μM ThT was added. Fluorescence
780 emission was measured within 5 min of ThT addition using a Tecan Infinite M1000 Pro
781 plate reader (excitation wavelength λ_{ex}=450 nm, emission wavelength λ_{em}=480 nm). The
782 measurements were performed in triplicate and the results are shown in Figure S6.

783 **Cryo-EM sample preparation**

784 Freshly extracted fibrils (water fraction 3) were deposited on the grids immediately upon
785 isolation. UltrAuFoil R 1.2/1.3 copper 300 mesh grids (Quantifoil, N1-A14nAu30-50) were
786 glow-discharged for 45 sec at 15 mA using a PELCO easiGlow glow discharge system to
787 apply a negative charge to their surface. A 3 ml sample was deposited on the grid surface
788 and immediately blotted for 3 sec with a blot force of 3 and plunge-frozen in liquid ethane
789 using a Vitrobot Mark IV apparatus (Thermo Fisher) set to 100% humidity and 4°C.

790 **Cryo-EM data collection**

791 A cryo-EM dataset of AL-224L amyloid was collected at the Boston University Cryo-EM
792 Core Facility using a Glacios II at 200 kV equipped with a Falcon 4i direct electron detector,
793 Selectris energy filter, and fringe-free imaging. A dataset of 10,309 exposures was
794 collected using Thermo Fisher EPU in counting mode and recorded in the Electron Event
795 Representation (EER) format using a magnification of 130,000x, pixel size of 0.90 Å, total
796 dose of 40 $e^{-}Å^{-2}$, dose rate of 10.82 e^{-} per pixel per second, defocus range of −0.8 to
797 −2.5 µm, and energy filter slit width of 10 eV. The imaging rate was approximately 550
798 exposures per hour. A multishot imaging strategy was used to collect four exposures per
799 grid hole, utilizing beam image shift to move between acquisition areas. Grid screening of
800 the amyloid sample prior to data collection revealed fibrils more abundant near the edges
801 of the foil holes. To maximize the number of fibrils visible in each exposure, the corner of
802 each of the four acquisition areas was positioned partially over the gold film surface.

803 **Cryo-EM data processing**

804 The dataset was processed in cryoSPARC v4.5.1[59]. Exposures were imported with an
805 EER upsampling factor of 2 then cropped by one-half back to their original resolution using
806 patch motion correction. The contrast transfer function (CTF) correction was performed
807 with 'patch CTF estimation'. Poor-quality micrographs were removed, yielding 7,076 high-
808 quality micrographs. Template-free 'Filament tracer' and 'inspect picks' were used to pick
809 filament segments with a separation distance of 45 Å from a 1000 micrograph subset of
810 the data. Particles were extracted at a box size of 896 px and Fourier-cropped to 448 px
811 using 'extract mics' to yield a partial uncleaned particle stack (71,140 particles). A set of
812 2D templates was generated with '2D classification' and 'select 2D'. The 2D templates
813 were used with 'filament tracer' and 'inspect picks' to pick filament segments with a
814 separation distance of 45 Å from the full 7,706 micrograph dataset. Particles were
815 extracted at a box size of 900 px and Fourier-cropped to 450 px using 'extract mics' to
816 yield a full uncleaned particle stack (421,024 particles). Particle cleaning was performed
817 primarily using 2D classification. Three rounds of '2D classification' and 'select 2D' were
818 performed to remove junk particles and double protofilaments yielding a partially cleaned
819 particle stack (236,744 particles). An initial EM map of single protofilament AL-224L was
820 generated using 'ab-initio reconstruction' by asking for an output of three volumes and
821 selecting the best quality volume. An initial refinement was performed with 'helix refine' to
822 obtain a particle stack with estimated 3D alignments. The partially cleaned, partially

823 aligned particle stack was extracted again at a smaller box size of 400 px. These particles
824 from a smaller box size were cleaned one last time using ‘2D classification’ and ‘select 2D’
825 to yield a cleaned particle stack (214,351 particles).

826 A 3D map of the cleaned particle stack was generated with ‘reconstruct only’ and was
827 used as an input for ‘helix refine’. ‘Helix refine’ was used to generate an initial refined EM
828 map of the single-filament amyloid. In this first ‘helix refine’ job, symmetry
829 searching/enforcement was disabled, and the initial model was lowpass filtered to a
830 resolution of 8 Å. The output volume, which was used as an input volume in the next step,
831 showed bumps that correspond to stacked β-sheets. These β-sheet features enabled the
832 symmetry search utility in the next step to find the correct helical rise/twist values. ‘Helix
833 refine’ was performed again with symmetry search/enforcement enabled to produce a
834 Symmetry Enforced Structure. The initial model was lowpass filtered to 4.5 Å, and the twist
835 and rise parameters were searched over -5.2° to 3.2° and 0.8 Å to 8.8 Å, respectively.
836 Helical symmetry search and enforcement was set to begin at 4 Å to ensure that symmetry
837 averaging was applied only after the β-sheet separation along the fibril z-axis was visible.
838 The symmetry was calculated to have a helical rise of 4.86 Å, which is typical of amyloid
839 fibrils, and a twist of 1.20°. Individual particle CTF and individual particle motion was
840 corrected with ‘reference-based motion correction’. The final EM map was generated with
841 a final round of ‘helix refine’ with symmetry search/enforcement enabled (214,100
842 particles, 2.92 Å, sharpening B-factor of -25.8).

843 **Cryo-EM model building**

844 An atomic model for AL-224L amyloid was built and refined against the sharpened EM
845 map. Initially, a single polyalanine chain was built into a central section across the fibril z-
846 axis and manually adjusted using Coot[60]. The individual residues were mutated to
847 correspond to the amino acid sequence of AL-224L determined by mass spectrometry.
848 The amino acid assignment within the EM map was determined by carefully examining
849 the path of the backbone, the position of the well-defined disulfide bond, C22-C91, and
850 the strong EM density for side chains that often corresponds to aromatic residues.
851 Residues 42-58 and 105-216 were not modeled because of weak EM density, suggesting
852 conformational heterogeneity in these segments.

853 The single molecular layer was duplicated to create a five-layer model. The replicated
854 molecules were rigid fit within the EM map above and below the original strand using the

855 fit-in-map function in ChimeraX[61]. The model was further refined in PHENIX[62] using
856 phenix.real_space_refine[63]. The β-sheet secondary structure, disulfide bond, and non-
857 crystallographic symmetry were manually defined in PHENIX to help guide the refinement
858 and impose identical conformations across all five molecular layers. The model statistics
859 and map-model fit were iteratively improved with multiple rounds of real-space refinements
860 in PHENIX and manual adjustments in Coot. To prevent the model from getting trapped in
861 the wrong conformation at an early stage, initial real-space refinement runs were
862 performed at lower map weight values, while final real space refinement runs were
863 performed at higher map weight values. The model was validated using the cryo-EM
864 Comprehensive Validation module in PHENIX running MolProbity[64].

865 To determine the handedness of the cryo-EM map and model of AL-224L amyloid fibrils,
866 we generated a highly sharpened cryo-EM map (sharpening B-factor of -200) and checked
867 if the orientation of the backbone carbonyl atoms matched the corrugation of the backbone
868 cryo-EM density. This approach was described for amyloid-like FUS fibrils[43] and is suitable
869 for high-resolution cryo-EM maps. In our structure of AL-224L amyloid, the right-handed
870 map and model had a much better map-model fit than the left-handed map and model.

871 Figures were generated with ChimeraX[61].

872

873 **Validation of additional densities using false discovery rate (FDR) thresholding**

874 To validate the significance of the three orphan densities seen in the cryo-EM map at the
875 internal and external sites, we generated a confidence map using FDR thresholding[37] with
876 default parameters and without incorporating local resolution and atomic model
877 information. We performed the map generation using the unmasked unsharpened AL-
878 224L cryo-EM map as the input and generated a figure viewed at a threshold of
879 0.99999999, equivalent to a 0.000001% false discovery rate for visible voxels
880 (Supplemental Fig. 1). The three densities were visible in the map indicating that their
881 probability of being noise was below 0.000001%.

882

883 **Methods References**

884 57. Prokaeva, T. *et al.* A novel substitution of proline (P32L) destabilises β2-microglobulin
885 inducing hereditary systemic amyloidosis. *Amyloid* **29**, 255–262 (2022).

886 58. Klimtchuk, E. S., Prokaeva, T. B., Spencer, B. H., Gursky, O. & Connors, L. H. In vitro co-
887 expression of human amyloidogenic immunoglobulin light and heavy chain proteins: a
888 relevant cell-based model of AL amyloidosis. *Amyloid* **24**, 115–122 (2017).

889 59. Punjani, A., Rubinstein, J. L., Fleet, D. J. & Brubaker, M. A. cryoSPARC: algorithms for
890 rapid unsupervised cryo-EM structure determination. *Nat Methods* **14**, 290–296 (2017).

891 60. Emsley, P., Lohkamp, B., Scott, W. G. & Cowtan, K. Features and development of Coot.
892 *Acta Crystallogr D Biol Crystallogr* **66**, 486–501 (2010).

893 61. Pettersen, E. F. *et al.* UCSF ChimeraX: Structure visualization for researchers,
894 educators, and developers. *Protein Sci* **30**, 70–82 (2021).

895 62. Liebschner, D. *et al.* Macromolecular structure determination using X-rays, neutrons
896 and electrons: recent developments in Phenix. *Acta Crystallogr D Struct Biol* **75**, 861–
897 877 (2019).

898 63. Afonine, P. V. *et al.* Real-space refinement in PHENIX for cryo-EM and crystallography.
899 *Acta Crystallogr D Struct Biol* **74**, 531–544 (2018).

900 64. Williams, C. J. *et al.* MolProbity: More and better reference data for improved all-atom
901 structure validation. *Protein Sci* **27**, 293–315 (2018).

902

903 **EXTENDED DATA**

Characteristics	AL-224	Reference range
Demographic features		
Gender	F	
Age, years	63	
Age at death, years	63	
Cause of death	sudden death	
Echocardiographic features		
Interventricular septal thickness (mm)	11	
Ejection fraction, %	60	
Laboratory parameters		
Bone marrow plasma cells, %	n/a	
LC restriction	λ	
SIFE	IgG+ λ FLC	
FLC κ	9.20	3.3–19.4
FLC λ	175.00	5.7–26.3
FLC ratio	0.05	0.26–1.65
Abnormal HLC, isotype	IgG	
IgG HLC κ	1.6	3.84–12.07
IgG HLC λ	8.49	1.91–6.74
IgG HLC ratio	0.19	1.12–3.21
UIFE	λ FLC	
BNP, pg/ml	126	0-176
Troponin I, ng/ml	0.046	<0.033
Serum creatinine, mg/dl	0.91	0.7–1.3
eGFR, ml/min/1.73 m^2	71	
24-h urine protein, mg	469	
Alkaline phosphatase, U/l	127	25–100
Organ involvement		
Cardiac	+	
Soft tissue	+	
Congo red positive histology		
Fat pad aspirate	+	
Bone marrow biopsy	+	

904

905 **Table S1**. **Demographic, clinical and laboratory characteristics of case AL-224 with AL amyloidosis at**
906 **initial evaluation.** Abbreviations: BNP, B-type natriuretic peptide; eGFR, estimated glomerular filtration rate;
907 FLC, free light chain; HLC, heavy light chain; Ig, immunoglobulin; LC, light chain; SIFE, serum immunofixation
908 electrophoresis; UIFE, urine immunofixation electrophoresis.

909

Accession	Description	Coverage [%]	# PSMs	# Unique Peptides	# AAs	MW [kDa]
P12883	Myosin-7 OS=Homo sapiens OX=9606 GN=MYH7 PE=1 SV=5	76	841	133	1935	223
P13533	Myosin-6 OS=Homo sapiens OX=9606 GN=MYH6 PE=1 SV=5	50	521	3	1939	223.6
AL-224L	Amyloidogenic LC sequence AL-224L OS=Homo sapiens	74	373	40	218	23.3
Q8WZ42	Titin OS=Homo sapiens OX=9606 GN=TTN PE=1 SV=4	7	257	224	34350	3813.7
P62736	Actin, aortic smooth muscle OS=Homo sapiens OX=9606 GN=ACTA2 PE=1 SV=1	70	187	39	377	42
P12882	Myosin-1 OS=Homo sapiens OX=9606 GN=MYH1 PE=1 SV=3	25	157	4	1939	223
P35609	Alpha-actinin-2 OS=Homo sapiens OX=9606 GN=ACTN2 PE=1 SV=1	44	112	42	894	103.8
P60709	Actin, cytoplasmic 1 OS=Homo sapiens OX=9606 GN=ACTB PE=1 SV=1	47	110	5	375	41.7
P06576	ATP synthase subunit beta, mitochondrial OS=Homo sapiens OX=9606 GN=ATP5F1B PE=1 SV=3	70	99	58	529	56.5
Q14896	Myosin-binding protein C, cardiac-type OS=Homo sapiens OX=9606 GN=MYBPC3 PE=1 SV=4	38	93	64	1274	140.7
P12111	Collagen alpha-3(VI) chain OS=Homo sapiens OX=9606 GN=COL6A3 PE=1 SV=5	16	76	53	3177	343.5
P25705	ATP synthase subunit alpha, mitochondrial OS=Homo sapiens OX=9606 GN=ATP5F1A PE=1 SV=1	54	63	41	553	59.7
P17540	Creatine kinase S-type, mitochondrial OS=Homo sapiens OX=9606 GN=CKMT2 PE=1 SV=2	39	57	30	419	47.5
P04004	Vitronectin OS=Homo sapiens OX=9606 GN=VTN PE=1 SV=1	25	52	17	478	54.3
Q08043	Alpha-actinin-3 OS=Homo sapiens OX=9606 GN=ACTN3 PE=1 SV=2	14	52	3	901	103.2
P06727	Apolipoprotein A-IV OS=Homo sapiens OX=9606 GN=APOA4 PE=1 SV=4	55	45	37	396	45.3
P02511	Alpha-crystallin B chain OS=Homo sapiens OX=9606 GN=CRYAB PE=1 SV=2	65	36	23	175	20.1
Q9Y2K3	Myosin-15 OS=Homo sapiens OX=9606 GN=MYH15 PE=1 SV=6	3	32	2	1926	222
P12109	Collagen alpha-1(VI) chain OS=Homo sapiens OX=9606 GN=COL6A1 PE=1 SV=3	19	29	20	1028	108.5

P48735	Isocitrate dehydrogenase [NADP], mitochondrial OS=Homo sapiens OX=9606 GN=IDH2 PE=1 SV=2	33	28	15	452	50.9
P07437	Tubulin beta chain OS=Homo sapiens OX=9606 GN=TUBB PE=1 SV=2	34	28	3	444	49.6
P68371	Tubulin beta-4B chain OS=Homo sapiens OX=9606 GN=TUBB4B PE=1 SV=1	38	28	4	445	49.8
P17661	Desmin OS=Homo sapiens OX=9606 GN=DES PE=1 SV=3	33	27	15	470	53.5
P12814	Alpha-actinin-1 OS=Homo sapiens OX=9606 GN=ACTN1 PE=1 SV=2	14	27	6	892	103
P55809	Succinyl-CoA:3-ketoacid coenzyme A transferase 1, mitochondrial OS=Homo sapiens OX=9606 GN=OXCT1 PE=1 SV=1	28	27	19	520	56.1
P54296	Myomesin-2 OS=Homo sapiens OX=9606 GN=MYOM2 PE=1 SV=3	15	23	19	1465	164.8
P21796	Non-selective voltage-gated ion channel VDAC1 OS=Homo sapiens OX=9606 GN=VDAC1 PE=1 SV=2	57	22	16	283	30.8
P12110	Collagen alpha-2(VI) chain OS=Homo sapiens OX=9606 GN=COL6A2 PE=1 SV=4	16	21	18	1019	108.5
P45880	Voltage-dependent anion-selective channel protein 2 OS=Homo sapiens OX=9606 GN=VDAC2 PE=1 SV=2	34	21	10	294	31.5
P02649	Apolipoprotein E OS=Homo sapiens OX=9606 GN=APOE PE=1 SV=1	34	21	15	317	36.1

Table S2. Top 30 master proteins identified with at least two unique peptides of heart-tissue extracted fibrils by LC-MS/MS.

Abbreviations: PSM, peptide-spectrum match; #AAs, number of amino acids in full-length protein; MW, molecular weight. The proteins are ranked according to the number of PSMs. Fibril-forming protein AL-224L (pink), collagen VI chains a1, a 2 and a 3 (green), and the amyloid signature proteins apoA-IV and apoE (orange) are highlighted. Serum amyloid P-component was detected in low abundance (#39, not shown). The data normalization using normalized spectral abundance factor (NSAF) values demonstrated AL-224L as the top identified protein (data not shown). To calculate the NSAF value for each protein, the spectral counts were divided by the protein length (PSM/#AAs) and the sum of all PSM/#AA values was divided by the number of all identified proteins as previously reported (Neilson KA, Keighley T, Pascovici, D, Cooke B, Haynes PA. (2013) Label-Free Quantitative Shotgun Proteomics Using Normalized Spectral Abundance Factors. Methods Mol Biol. 2013:1002: 205-222).

LC sub-family	PDB ID	ΔG, kcal/mol
λ3	9FAA	-33.7
λ3	9FAB	-33.4
λ3	9FAC	-34.2
λ3	8R47	-26.4
λ3	9EME	-25.5
λ1	7NSL	-26.6
λ1	6IC3	-24.2
λ3	6Z1O	-21.5
λ3	6Z1I	-20.4
λ6 AL55 renal	8CPE	-23.3
λ6 AL55 cardiac	6HUD	-20.2
λ6 AL-224L cardiac	**9OKA**	**-18.0**
λ6 germline	6HUD	-18.6
λ6 germline	9OKA	-22.1

Table S3. Solvation energy calculated for the available amyloid structures of AL LCs.
ΔG values represent free energy change upon interface formation between two fibril layers, which was estimated using Protein Interfaces, Surfaces and Assemblies (PDBePISA) server, https://www.ebi.ac.uk/msd-srv/prot_int/cgi-bin/piserver. Bottom two rows list hypothetical values for the λ6-LC germline sequence placed in the amyloid structure of cardiac AL55 LC (PDB: 6HUD) or cardiac AL-224L (PDB: 9OKA). Mutations to restore the germline sequence were introduced using the Swiss-PdbViewer software, https://spdbv.unil.ch/ and the structure was energy-minimized to relieve steric clashes.

932

933

Sample	SCFA	Recovery	Recovery
	μM	**μM**	**%**
SCFA	19.97		
NEFA	0		
SCFA + NEFA	21.89	21.89	109.6
Fr3	**38.71**		
Fr3 + NEFA	36.75	36.75	95.0
Fr3 + SCFA	56.92	18.21	91.1
Fr3 + SCFA + NEFA	88.26	51.49	74.9

934

935 **Table S4. Short chain fatty acid content in the amyloid-containing tissue extracts (fraction 3) measured**
936 **by ELISA and assay validation.**
937 Abbreviations: SCFA - short chain fatty acid; NEFA – non-esterified fatty acid; Fr3 – tissue-extracted fraction
938 3 used for cryo-EM analysis of amyloid. The experimental details are reported in Methods.

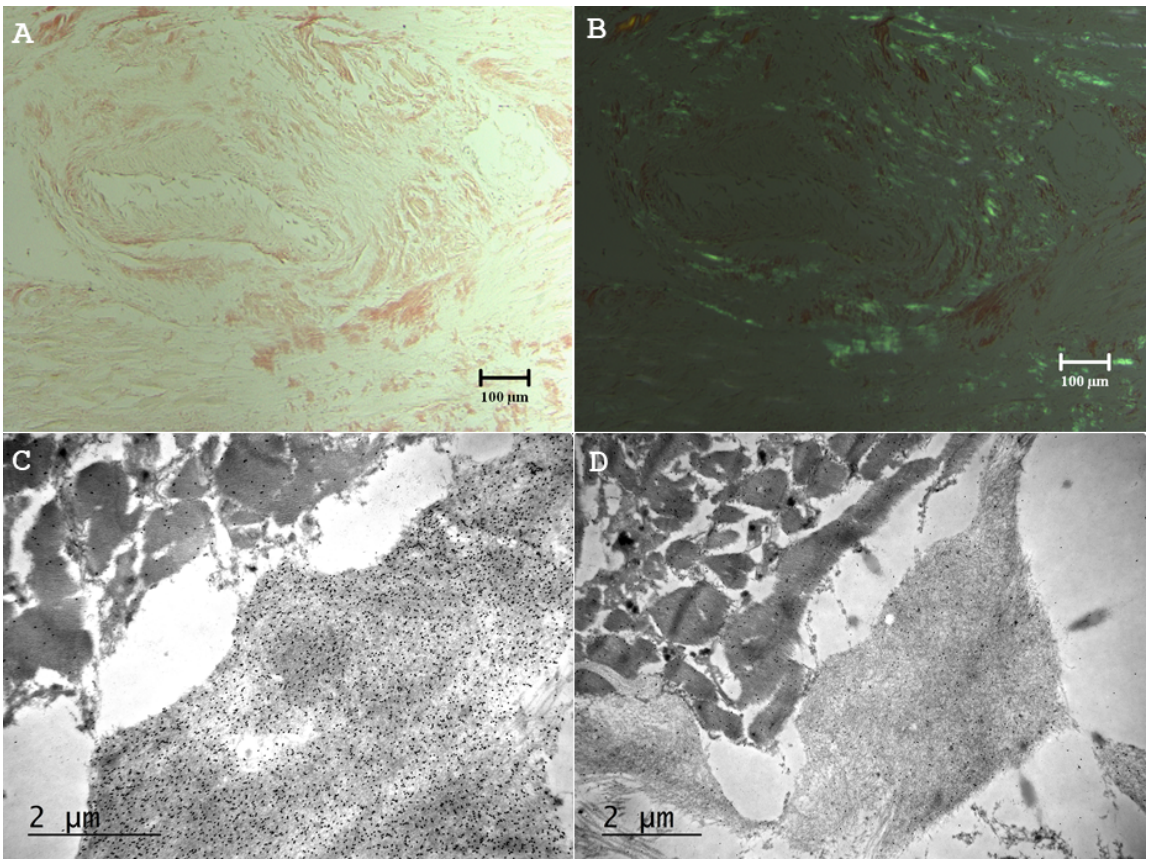

Figure S1. Histological analyses of the autopsied cardiac tissue in case AL-224.
A, Light microscopy images of Congo red-stained cardiac tissue indicate amyloid deposits. Original magnification ×100. **B**, Areas in panel A viewed by polarized microscopy show amyloid deposits with characteristic green birefringence. Original magnification ×100. **C, D**, Electron micrographs of autopsied cardiac tissue show haystack-like organization of amyloid fibrils in the extracellular space. Immunogold labeling demonstrates numerous electron dense deposits with antibody directed against immunoglobulin λ-LC (original magnification ×20,000, **(C)** and no immunoreactivity with antibody directed against immunoglobulin κ-LC (original magnification ×15,000, **(D)**.

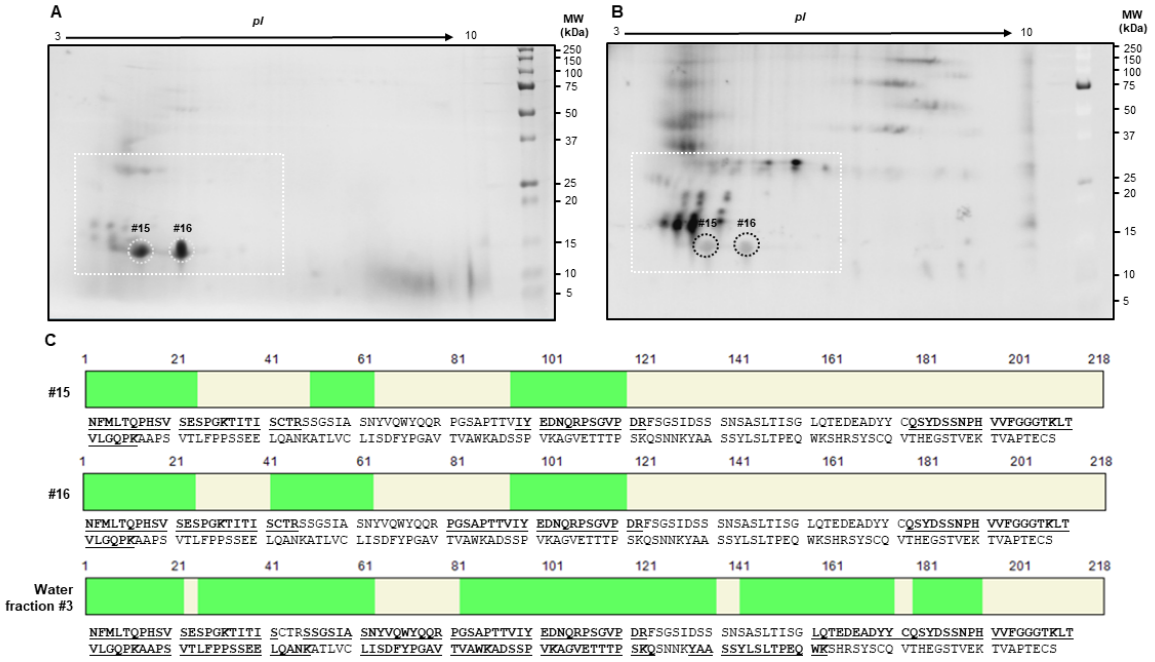

Figure S2. Analysis of AL-224 proteins in water fraction 3 of cardiac tissue fibril extract using 2D SDS-PAGE, 2D western blotting and LC-MS/MS.

A, Coomassie-stained gel and **B**, the corresponding 2D western blot probed with a primary anti-human λ light chains antibody. Two most prominent spots are circled and marked #15 and #16. These spots were excised and analyzed by LC-MS/MS, along with the entire water fraction 3. **C**, Amino acid sequence of AL-224L shows the position (in green) and sequence (underlined bold) of the peptides identified in spots #15, #16 and in the entire water fraction 3 (indicated).

958

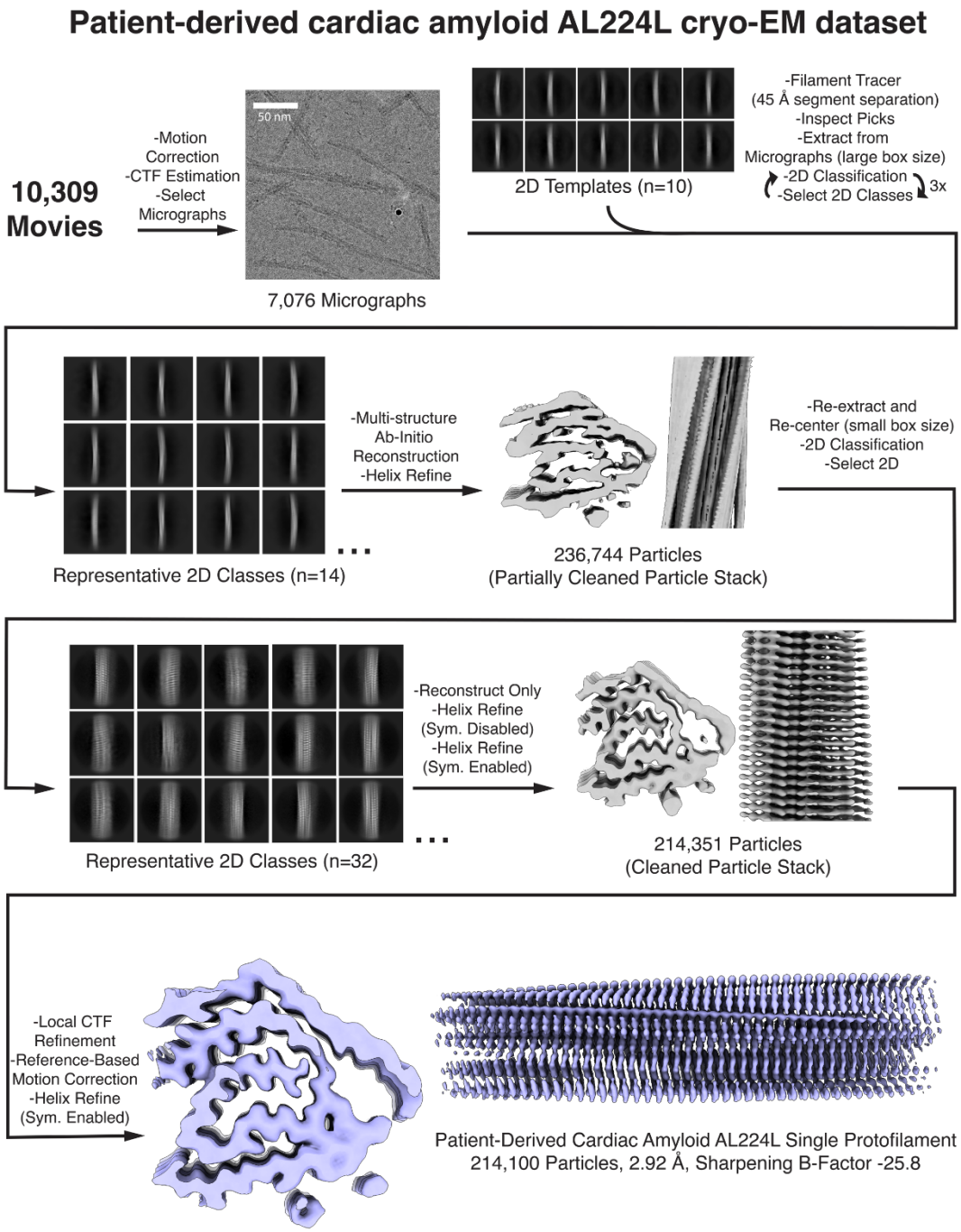

959 **Figure S3. Cryo-EM data processing workflow.**
960 General processing pipeline to generate an EM map of an AL-224L single-filament amyloid polymorph.

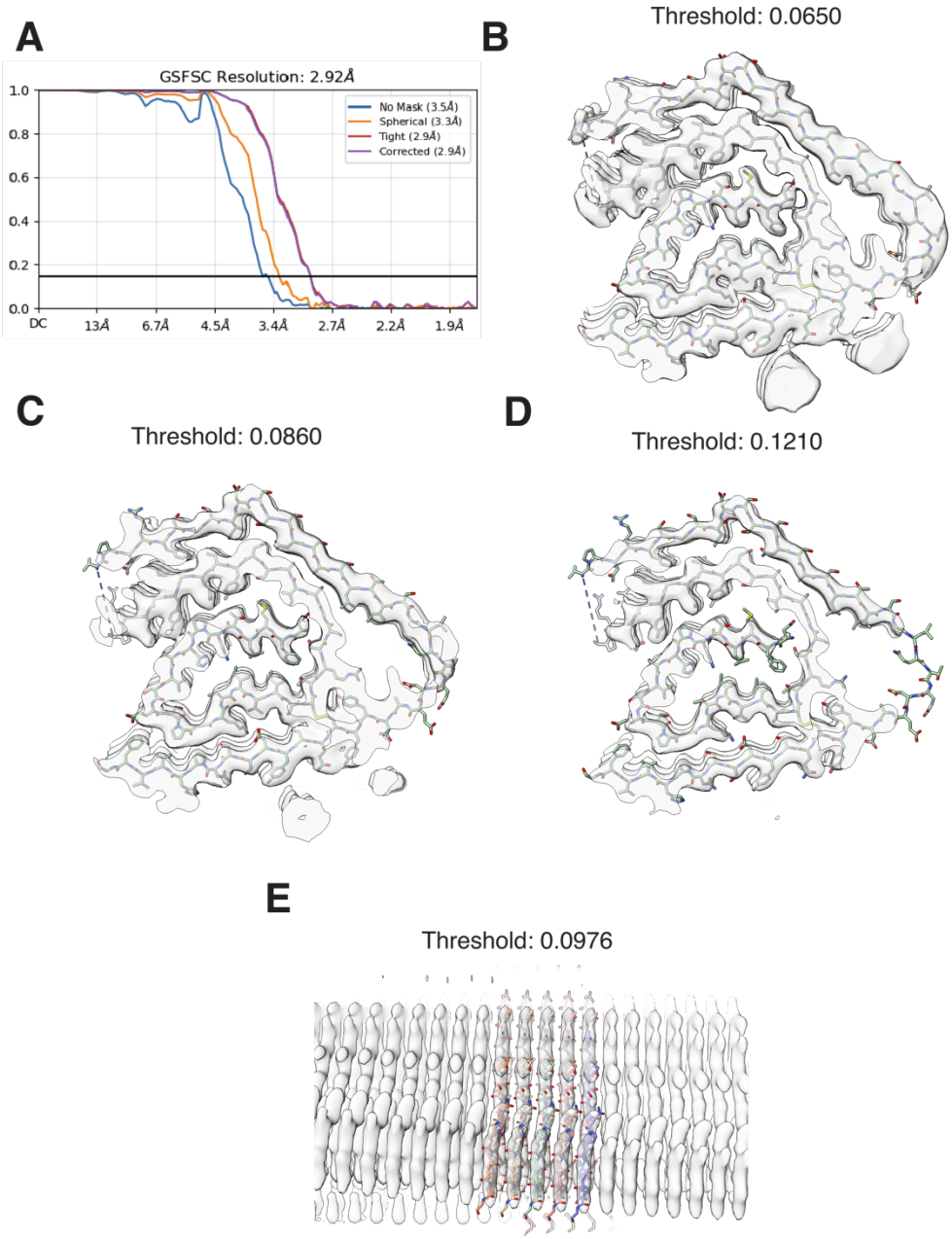

Figure S4. **Global resolution and map-model fit evaluation of amyloid structure.**
A, Fourier shell correlation (FSC) plot at a gold standard 0.143 cutoff of cardiac amyloid AL-224L.
B-E, AL-224L model superimposed over the EM map to show the map-model fit at EM map at thresholds as indicated.

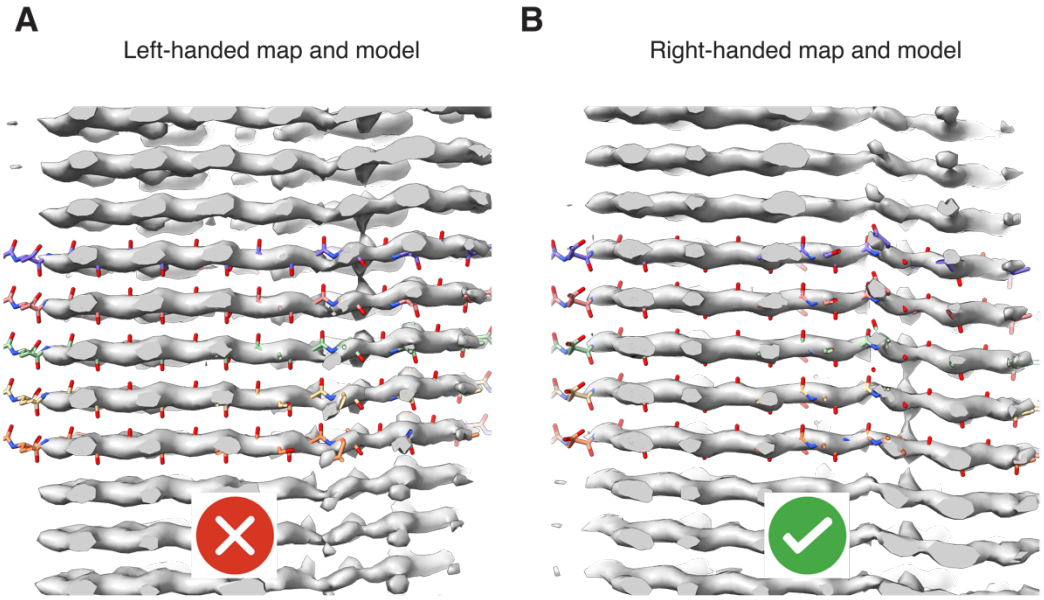

Figure S5. **Backbone corrugations reveal the AL-224L amyloid to be right-handed.**
A, Slice-view showing a superimposition of the left-handed amyloid model over the highly sharpened left-handed amyloid map. Green check icon indicates that the right-handed map and model have correct handedness. **B,** Slice-view showing a superimposition of the right-handed amyloid model over the highly sharpened right-handed amyloid map. Green check icon indicates that the right-handed map and model have correct handedness.

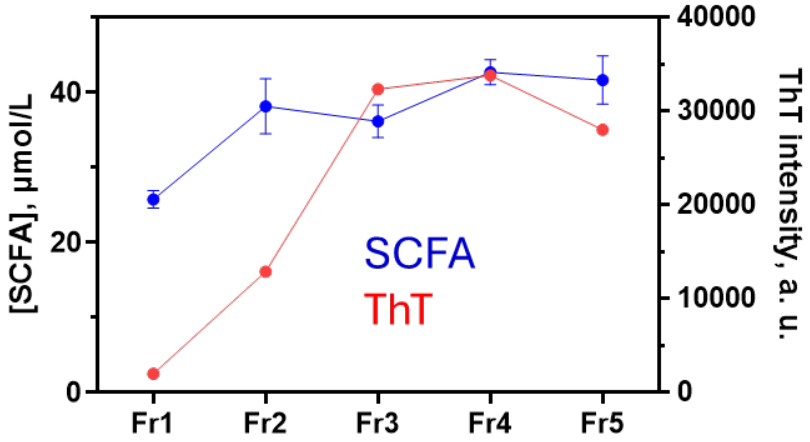

973

974 **Figure S6. Amyloid and short chain fatty acid (SCFA) content in fractions 1-5 extracted from autopsied**
975 **cardiac tissue AL-224.**
976 SCFA were measured by ELISA in technical and biological duplicates; mean values ± SEM are shown.
977 Amyloid was assessed by measuring fluorescence emission of a diagnostic dye thioflavin T (ThT) that shows
978 increased fluorescence upon binding to amyloid. Methods provide experimental details.

SUPPLEMENTAL DATA

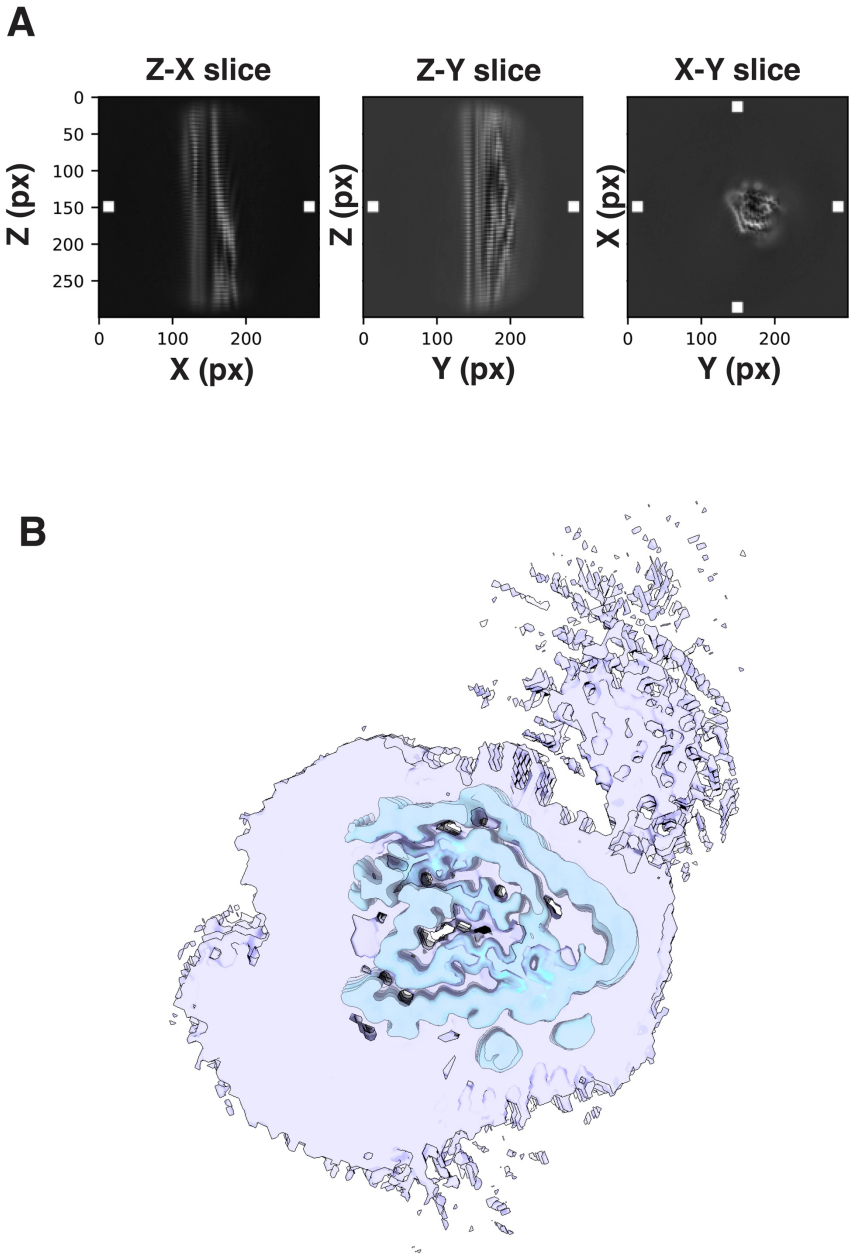

Supplemental Figure 1. **False Discovery Rate (FDR) Threshold Confidence Map.**
A, Slice-views of the unsharpened AL-224L amyloid input EM map to FDR thresholding. White boxes indicate the 3D area that was sampled to produce a noise estimate to generate a confidence map. **B,** Traditional unsharpened AL-224L amyloid EM map (blue) within an unsharpened AL-224L amyloid EM confidence map (purple) generated with FDR thresholding and viewed at a threshold of 0.99999999, equivalent to a 0.000001% false discovery rate for visible voxels.